The Growth and Characterization of Cesium-Antimonide Photocathodes for Optical Near Field Electron Microscopy

Benali, Dalal

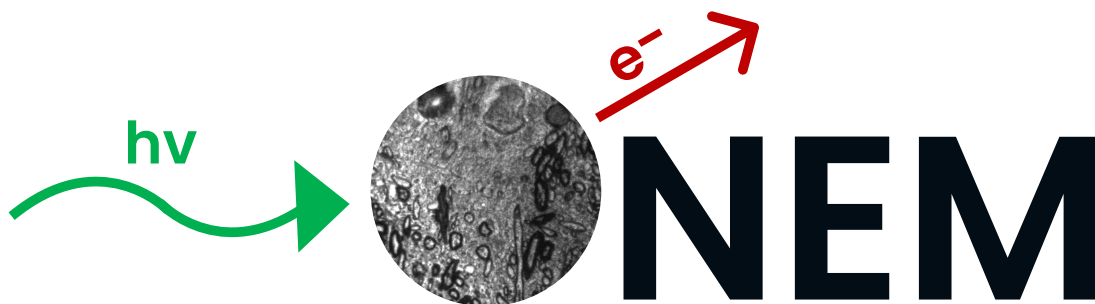# The Growth and Characterization of Cs$_3$Sb Photocathodes for Optical Near Field Electron Microscopy

The Growth and Characterization of Cs$_3$Sb Photocathodes for Optical Near Field Electron Microscopy

D. Benali

Huygens-Kamerlingh Onnes Laboratory, Leiden University
P.O. Box 9500, 2300 RA Leiden, The Netherlands

April 26, 2025

Abstract

Emerging techniques for high-resolution biological and chemical imaging at the nanoscale are instrumental for addressing existing trade-offs in spatial resolution, imaging speeds and sample damage. The introduction of optical near field electron microscopy (ONEM) offers a solution for some of the limitations in existing microscopy techniques, by capturing the high-resolution spatial information of light that is scattered in the near field of a sample. Through positioning a photocathode in the near field regime, the scattered light can be converted to electrons and imaged with a low energy electron microscopy (LEEM), thus enabling super-resolution without damage. This thesis explores the design and realization of a dedicated ONEM photocathode growth setup inside the 'ESCHER' LEEM at Leiden University, consisting of a thermal co-evaporator, quantum efficiency setup, quartz crystal monitor and sample heater. We then use this setup to evaporate and characterize cesium-antimonide thin films to investigate how the growth conditions can be tuned to optimize the photoemission quality. The aim is to create ultra-smooth, ultra-thin layers with a high quantum efficiency and a low work function. Through this project, we lay the foundation for dedicated ONEM photocathode growth, which will enable further advancements in the effort to establish ONEM as a viable high-resolution imaging technique.

Contents

5   Outlook and Conclusion   **43**

Introduction

Capturing surfaces and interfaces at the nanometric level is essential for progress in fields like biology and chemistry. For instance, understanding how ligands interact with cell membrane proteins is a key step in developing new pharmaceutical drugs and advancing biomedical research [1]. Imaging at this scale also plays a critical role in studying the reaction mechanisms of nanocatalysts, which are important for the energy and environmental industries [2]. Naturally, there are various other biological and chemical processes that are suited for high-resolution imaging, such as protein dynamics during cellular apoptosis and the structural organization of biomolecules in individual cells [3, 4]. As we gain new insights into these processes, the demands for advanced microscopy techniques evolve accordingly.

Historically, the Abbe diffraction limit has restricted conventional imaging techniques from resolving features smaller than a few hundred nanometers [5]. The establishment of far field optical super-resolution microscopy (SRM) around the turn of the century overcame this limitation, with techniques like single-molecule localization microscopy (SMLM) achieving lateral resolutions below 10 nm [6]. This breakthrough shifted the focus from optimizing the resolution, to navigating the trade-offs that are inherent to nanoscale bio- and chemical imaging. Specifically, the spatial and temporal resolution, the imaging depth and the level of photodamage form a balance that determines performance and applicability of certain super-resolution imaging techniques. For example, while SMLM offers precise xy-localization, it suffers from poor z-axis resolution, slow imaging speed, and the need for molecular labeling. The latter two make SMLM unsuitable for dynamical biological imaging, such as for live-cells. Structured illumination microscopy offers better temporal resolution and imaging depth, but with a lateral resolution that is ten times higher than that of SMLM [7].

Beyond optical methods, other ways of achieving nanometric resolution include scanning force microscopy and electron microscopy. Atomic force microscopy, a popular scanning method, can distinguish feature sizes between 1 and 10 nm in a label-free, minimally invasive manner. However, its sequential scanning technique slows down the process of producing high-resolution images. Similarly, electron microscopes, such as scanning transmission electron microscopes, offer exceptional lateral resolution, even resolving single atoms. Unfortunately, the temporal resolution is not high enough for dynamic imaging, and the high-energy beams of most electron micro-

scopes cause significant damage to biological and chemical samples [8]. Additionally, these techniques necessitate elaborate staining and fixation processes in order to be imaged. Although cryo-electron microscopy mitigates some of this damage by rapidly freezing samples in their native state, it restricts the technique to capturing only static snapshots.

Resolving the trade-offs between resolution and damage is essential in overcoming the current limitations in optical and electron microscopy, and can be achieved by combining different techniques into one. In 2021, this was realized with the introduction of optical near field electron microscopy (ONEM), which merges low-energy electron microscopy (LEEM) and optical near field scattering to form a novel solution for biological and chemical nanoscale imaging [9]. ONEM utilizes the photoelectric effect to turn visible light, which is elastically scattered from an illuminated sample, into electrons. The latter are subsequently detected by the LEEM, enabling high-resolution imaging without the risk of sample damage. Aside from being label-free and non-invasive due to the use of visible light, ONEM has the potential for dynamic measurements of sensitive sample interfaces through wide-field imaging. Furthermore, by employing specialized liquid cells that can withstand the high vacuum environment of the LEEM, they do not have to undergo staining or freezing processes.

Despite its promising advantages, there are several obstacles that prevent ONEM from becoming a viable and established method. Among these is the development of an effective photocathode, which involves addressing technical challenges that relate to its photoelectric conversion efficiency, surface smoothness, film thickness and fabrication reproducibility. This thesis aims to overcome these challenges by designing and assembling an experimental setup for the evaporation of alkali-antimonide photocathodes onto samples that are relevant for ONEM. Additionally, by establishing an effective and reproducible growth protocol, we attempt to optimize and balance the multiple parameters that affect the quality of the photocathodes. In doing so, we seek to improve the feasibility and potential of ONEM as an emerging microscopy technique.

The structure of this thesis is as follows: Chapter 2 in provides background knowledge on the merging of LEEM and near field optics, as well as the basics of photocathodes and the photocathode characteristics that are required for ONEM. Following this, Chapter 3 is used to identify the design requirements for the different components of the evaporation setup and explain the assembly. Additionally, it establishes a photocathode growth protocol that is used throughout the project. The results of the photocathode growth are presented and discussed in Chapter 4. Specifically, this chapter aims to characterize the growth and effectiveness of the photocathodes, and addresses which growth protocols can be used to optimize and balance the different parameters that determine the quality of the photocathodes. Finally, Chapter 5 addresses the future steps towards ONEM, focusing on the improvement of the photocathodes, and provides a conclusion to the thesis.

Theory and Characterization of ONEM Photocathodes

ONEM serves as an extension of LEEM by utilizing its electron detection setup and combining it with a photon source, which emits light in the visible wavelength range. In between those two components lies the main focus of the project: The photocathodes that convert the scattered photons into electrons via the photoelectric effect. Under certain conditions, these electrons can reach the photocathode surface and travel into the vacuum of the LEEM, allowing for their subsequent detection and imaging. In order to create functioning photocathodes and improve their effectiveness, it is therefore essential to understand those conditions and the parameters that influence them. This chapter gives an overview of the setup design and general workings of the LEEM and ONEM, followed by a discussion of the working principles of photocathodes. In particular, we discuss alkali-antimonide thin films, which are popular in photocathode research due to their high conversion efficiency and relatively straightforward growth procedure [10].

2.1 Microscopy Essentials

In conventional LEEM, an electron source illuminates a sample with low-energy electrons. These are then either reflected, scattered or absorbed at the sample surface. The electrons that leave the sample follow a path that leads to a detection setup. Although the first half of the travel path of the electrons is replaced in ONEM, conventional LEEM is still used for the characterization of the photocathodes that are grown during this project. Therefore, the next section explains how the 'ESCHER' LEEM, located in the experimental lab of Leiden University, works.

2.1.1 Aberration-Corrected Low-Energy Electron Microscopy

As the name suggests, low-energy electron microscopes use electrons with a low energy, typically below 100 eV, to probe samples and record their surfaces. Inside materials, the electrons have a short inelastic mean free path that makes the LEEM especially applicable to surface imaging. Another important characteristic of the LEEM is the

controllability of the landing energy, which is achieved by creating potential differences between certain components in the system. This works in the following way: A cold field emission gun creates an electron beam with an electron kinetic energy of 15 keV, which is deflected by a magnetic prism to an electrically grounded objective lens. 1.5 mm behind the lens lies a sample that is biased at a voltage of $V = V_0 + V_s$. V_0 is typically set at -15 kV, matching the electron gun voltage. V_s can be tuned during measurements to create a potential difference between the gun and the sample. In the approach to the sample, the incoming beam is decelerated by an electrostatic field between the lens and the sample, resulting in an electron landing energy E_0 that ranges between -100 and 100 eV [11].

For negative E_0, the electrons are redirected back to the lens before reaching the sample surface. This leads to the mirror mode, where the reflectivity is equal to unity. The landing energy can be increased to positive values by adjusting V_s, enabling the interaction of the electrons with the sample surface. Specifically, $E_0 = 0$ indicates a mirror mode transition (MMT), identified by a significant reduction in the measured reflectivity [12]. The MMT also corresponds to the vacuum energy E_{vac}, the relevance of which becomes clear in section 2.2.1. Whether the interaction at landing energy E_0 results in the reflection, inelastic scattering or absorption of the electrons depends on both the material properties of the sample. For example, by adjusting V_s, it is possible to distinguish different layers of graphene, showing up as contrasted regions in the final image.

The electrons that travel back toward the objective lens are re-accelerated by the electrostatic field. Due to inelastic scattering, some electrons acquire a lateral motion that causes their trajectories to deviate from the main beam path. The resulting electron spread is a measure of the mean transverse energy (MTE), which depends on the roughness and local potential variations of the sample surface. While the electrostatic field bends the strayed electrons parallel to the main beam, their transverse momentum remains conserved. This leads to an increased beam divergence, thereby limiting the maximum spatial resolution [14]. While it is thus generally desirable to keep the
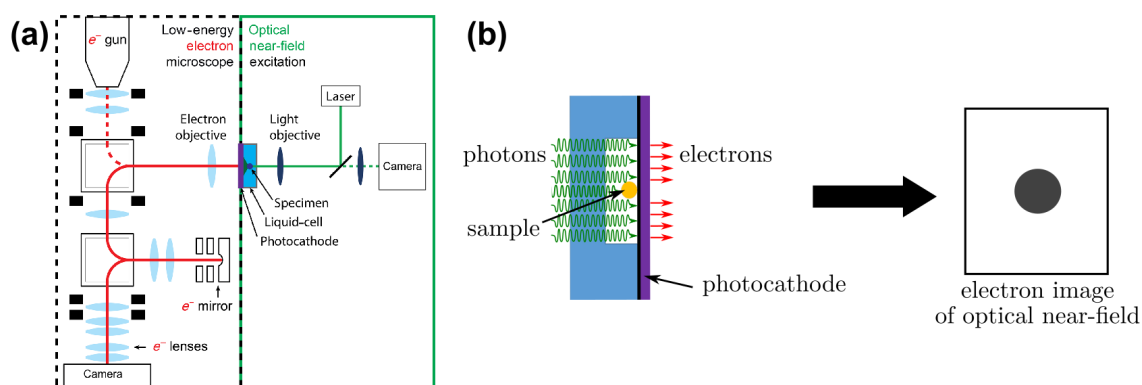
Figure 2.1: (a) Left: The red line represents the electron trajectory through the optical components of the LEEM. Right: Addition of ONEM optical components, which are use to illuminate laser light (green line) onto the back of a sample [9]. **(b)** A sample interfaced with a photocathode is illuminated by photons, which scatter from the sample and allow for the high-resolution spatial information in the near field to be converted into electrons via the photoelectric effect. [13].

MTE as low as possible, this is beyond the scope of this project.

Unique to the ESCHER-LEEM is the addition of an aberration-correction setup. The electron beam travels to a four-element electron mirror, which can effectively correct for the chromatic and spherical aberrations that are picked up from the objective lens, consequently pushing the resolution below 2 nm [11, 15]. Finally, the electrons are detected by a projector system. Aside from conventional LEEM, the system can be put in the diffraction mode (LEED), which provides additional information about the crystal structure. The complete electron trajectory of the LEEM is shown on the left-hand side of Fig. 2.1a as a red line that goes past each of the described components.

2.1.2   Optical Near Field Electron Microscopy

In ONEM, the electron gun is inactive. Instead, the sample is probed by photons that originate from a light source *behind* the sample. As a sample is illuminated with visible light from a laser, the photons that are elastically scattered carry information about the spatial distribution of the sample features. The trajectory of the photons is shown on the right-hand side of Fig. 2.1a, represented by the green line. In conventional optical microscopes, the scattered light propagates and is detected in the Fraunhofer regime, or the far field. Here, the Abbe diffraction limit dictates that the smallest resolvable feature size d is limited to about half the wavelength λ, depending on the numerical aperture NA:

$$d = \frac{\lambda}{2\text{NA}}.$$
(2.1)

The operating principle of ONEM instead relies on capturing the optical information in the near field, a short distance z from the sample. For $z \ll \lambda$, wave interactions cannot be approximated. The regime contains non-propagating fields, called evanescent fields, from which high-resolution spatial information can be extracted [16, 17]. By placing a photocathode at such a distance z, the photoelectrons that are generated from the scattered photons can capture these high-resolution details and deliver them to the rest of the LEEM optics (see Fig. 2.1b). Thus, ONEM can be used to bypass the Abbe diffraction limit [9].

This mechanism forms the basis for high-resolution near field imaging and is used in other techniques, such as scanning near field optical microscopy (SNOM) [18]. While similar to ONEM, SNOM employs a scanning tip to probe the near field, which makes it suffer from the same limitations as other scanning probe methods. ONEM, on the other hand, uses the LEEM to capture the entire field of view instantly, enabling dynamic imaging.

Of course, to implement dynamic imaging in future, the sample must be isolated from the harsh vacuum of the LEEM system. This is accomplished by using a liquid cell that interfaces with a thin film of photocathode material [9]. When the liquid cell is sufficiently thin − on the order of tens of nanometers − the separation between the photocathode and the sample is small enough to enable ONEM. Here, it is important to note that z is determined by the location of the outgoing photoelectrons, at the surface of the photocathode. The achievable resolution therefore depends on the thickness of

the photocathode film. However, the thin film layer also cannot be too thin, as this affects the maximum detectable signal strength.

Clearly, a deeper understanding of these trade-offs, along with other photocathode characteristics, is crucial for optimizing ONEM. The following section, 2.2, discusses how photocathodes work and the material properties that influence their performance.

2.2 Photocathode Basics

Photocathodes are materials that use the photoelectric effect to eject photoelectrons when they are illuminated with photons. Each photon carries an energy $h\nu$, where h is the Planck constant and ν is the photon frequency, that is transferred to the conduction electrons in the photocathode material upon absorption. If the energy of these excited electrons exceeds a certain threshold, defined by the vacuum energy E_{vac}, they gain the possibility to escape into the vacuum. Although this energy condition is then satisfied, there is an additional momentum condition that needs to be met in order for the electrons to *actually* enter the vacuum [19]. This photoelectron ejection process is explained further in section 2.2.1.

2.2.1 Work Function

The minimum energy required to reach the vacuum energy is determined by the work function Φ_{WF} of the photocathode, which is a material-dependent property [12]. Specifically, the work function is the minimum energy required to bring an electron near the Fermi level E_{F} to the vacuum level E_{vac}, expressed as

$$\Phi_{\text{WF}} = E_{\text{vac}} - E_{\text{F}}. \tag{2.2}$$

Fig. 2.2a shows a schematic drawing of this process. There are two ways to bridge the gap between E_{F} and E_{vac}: The first one is to increase the incident photon energy through the use of light with a shorter wavelength. However, since the purpose of ONEM requires the use visible light to prevent sample damage, we instead overcome the threshold by choosing a material with an inherently low work function. Alkali-metals, such as cesium (Cs), are often combined with antimony (Sb) atoms to grow alkali-antimonide thin films. This results in photocathodes that have a significantly lower Φ_{WF} than those of the separate atoms.

In the case that the work function is lower than the energy of an absorbed incident photon, i.e., $h\nu \geq \Phi_{\text{WF}}$, the excited electron becomes a "hot electron". For the hot electron to reach the vacuum, its momentum perpendicular to the vacuum-surface interface must be sufficient to overcome the surface potential barrier. Although this condition decreases the probability of photoelectron ejection, it has the advantage of protecting the sample from electron back-scattering due to the potential barrier.

Whether the hot electrons reach the surface, depends on the scattering events that occur within the material. The mean free path of the electrons is determined by both elastic and inelastic scattering processes. For elastic scattering, such as through interactions with phonons or impurities in the material, the electron energy remains nearly
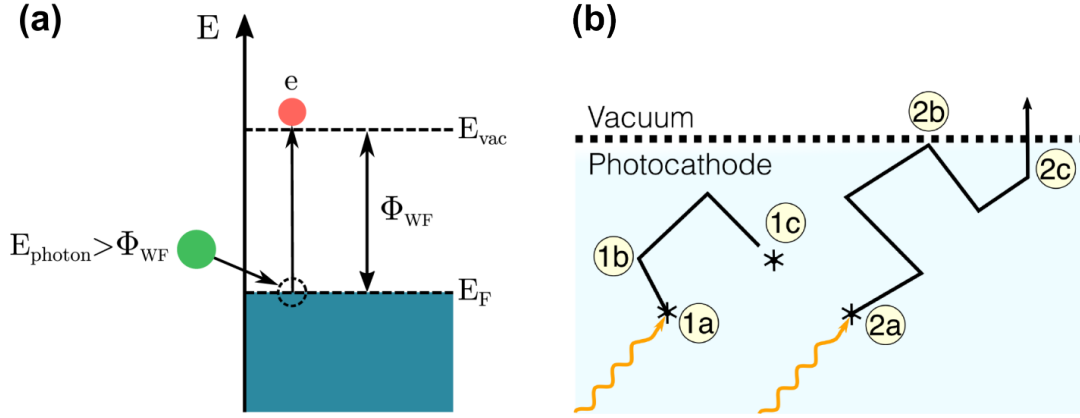
Figure 2.2: (a) An electron at the Fermi level can be excited by an incoming photon. If the photon energy exceeds the work function of the material, the electron can escape into the vacuum [13]. **(b)** Possible hot electron trajectories inside the material. Steps 1a-c show the excitation and (in)elastic scattering of an electron, causing it to lose energy and not leave the material. Steps 2a-c show electron excitation, reflection at the surface and subsequent escape into the vacuum [20].

constant. Its momentum, however, can be altered in the process. This can in turn prevent the electron from meeting the perpendicular momentum condition for escaping into the vacuum. Inelastic scattering processes involve energy loss through interactions with other electrons or phonons. This can decrease both the energy and momentum of the electron, increasing the probability that the electron energy falls back below the vacuum level and is re-absorbed by the photocathode material.

Clearly, these scattering events play a significant role in determining the probability of photoelectrons entering the vacuum of the LEEM chamber. This directly affects the photocathode conversion efficiency of incident photons to outgoing electrons, which is referred to as the quantum efficiency. The following section, 2.2.2, goes deeper into this concept.

2.2.2 Quantum Efficiency

Quantum efficiency (QE) of a photocathode is a measure of its effectiveness in converting incident photons into emitted photoelectrons. Specifically, it is defined as the ratio of the number of emitted electrons N_e and the number of incident photons N_γ,

$$QE = \frac{N_e}{N_\gamma} \times 100, \tag{2.3}$$

where the multiplication by 100 indicates that the QE is expressed as a percentage. The QE depends on several factors, including the work function and the internal scattering events. If the work function is significantly lower than the photon energy, the excited electrons gain more kinetic energy, and are less likely to fall back below the vacuum level due to inelastic scattering. Therefore, while ONEM requires Φ_{WF} to be at least lower than $h\nu$, it is favorable to minimize the photocathode work function as much as possible to increase the quantum efficiency.

Another way to maximize the quantum efficiency is by reducing the probability of interactions with impurities or grain boundaries that exist within the material. Consequently, promoting homogeneity and uniformity during the growth process of the photocathode layer can aid in the reduction of elastic scattering events. Additionally, this can reduce the potential roughness at photocathode surface, which causes local work function variations that lead to regions with a lower quantum efficiency.

Finally, the thickness of the photocathode layer plays a critical role in the obtainable quantum efficiency. Increasing the film thickness causes the creation of more interaction volume for the absorption of incident photons, which allows for the generation of a higher number of photoelectrons. Consequently, the QE initially rises as the photocathode grows thicker. However, this rise is limited by the mean free path of the excited electrons. Hot electrons generated deeper within the material undergo, on average, more scattering events, compared to those produced near the surface. When the thickness exceeds the electron mean free path, the probability of photoelectron ejection decreases, reducing the overall QE. Therefore, there exists an optimal thickness where photon absorption is sufficient to generate enough photoelectrons for a final sample image, while the distance remains short enough for electrons to escape into vacuum within their lifetime. As mentioned in section 2.1.2, the photocathode thickness is further limited as to preserve the obtainable resolution. This creates a trade-off between maximizing signal strength and maintaining resolution, making it necessary to find a balance. The determination of this optimal photocathode thickness is discussed in detail in section 2.3.2.

2.3 Photocathode Characteristics and Requirements

The alkali-antimonide photocathode forms the point where two imaging tools come together, converting scattered photons into detectable electrons. This places the functionality of the photocathodes at the center of our efforts to improve the conditions for ONEM, so that it can become a viable and reliable microscopy technique in the near future. Therefore, this section is concerned with investigating the optimal photocathode growth conditions by considering the criteria that can ensure their effectiveness for ONEM. This is done by identifying the parameters that influence the photocathode performance and using those to form design requirements for a dedicated growth setup. Here, we focus on the work function and quantum efficiency, which are critical for determining the photocathode effectiveness in ONEM.

2.3.1 Work Function

As mentioned in section 2.2.1, the aim is to reduce the photocathode work function as much as possible. Assuming that we illuminate the photocathode with green light, which has a wavelength of around 520 nm, the resulting photon energy is 2.39 eV. For the purpose of ONEM, the aim is to obtain a photocathode work function that is lower than this value. Naturally, further reducing the work function would allow for the use of light with a lower photon energy, expanding the range of usable wavelengths. Another benefit is a lower energy barrier for photoemission, which enhances the quantum efficiency of the photocathode.

Since the work function is a material property, the main influence is the addition of Sb deposition. Table 2.1 shows how a cesium-antimonide thin film has a work function that is 0.6 eV lower than that of Cs. Here, the 3:1 ratio of Cs and Sb, which refers to the stoichiometry, is a precise factor that determines the value of the work function of the compound. Therefore, introducing Sb deposition requires the addition of a method to monitor the deposition rates of both materials, allowing for precise control of the stoichiometry. The setup component that is used for this is a quartz crystal monitor, which is described in detail in section 3.2.3.

Table 2.1: The electron work functions (in eV) of Cs, Sb and Cs_3Sb thin films.

Material	Work function (eV)	Reference
Cs	2.1	[21]
Sb	4.0	[22]
Cs_3Sb	1.5 ± 0.1	[14]

Aside from the chemical composition of the compound, surface roughness and thin-film inhomogeneity can also influence the work function by introducing potential variations across the photocathode surface. These can locally alter the electronic properties, leading to Sb- and Cs-rich regions that contribute to an increased work function. One approach to minimize these effects is the simultaneous evaporation of Cs and Sb, which has been shown to significantly improve film homogeneity and near-atomic surface smoothness compared to sequential deposition [23, 24]. Therefore, we adopt co-evaporation as a for this project. The design and assembly of the co-evaporator are described in section 3.2.5.

Additionally, promoting epitaxial growth and enhancing the crystallinity can further optimize the film uniformity and reduce surface roughness. While using lattice-matched substrates, i.e. substrates whose lattice parameters resemble that of the grown film, is one method to achieve this [21, 25], it is not the focus of this project. Instead, we introduce substrate heating during deposition to aid in the reaction of Cs and Sb and encourage crystalline growth. While substrate heating is common in Cs_3Sb thin film growth, it is difficult to reproduce and optimize growth protocols that use substrate heating, partially due to the unreliability of the heater and recorded temperature. Other factors that contribute are the varying deposition rates and the pressure variations, making it difficult to establish an optimal substrate temperature [26]. Therefore, we aim for the substrate temperature of 80-90 C°, based on previous research work that has achieved near-atomically smooth, uniform Cs_3Sb growth [23, 25]. Section 3.2.5 discusses the design considerations and fabrication of the substrate heater further.

2.3.2 Quantum Efficiency

In order for the final LEEM image to be visually relevant, the photocathode has to emit enough photoelectrons to allow for sufficient brightness and contrast. The maximum signal strength of ONEM is mainly determined by the achievable quantum efficiency, which in turn is influenced by the stoichiometry and the film thickness. These parameters can be tuned and optimized, so that the change in the quantum efficiency can be

measured as a response. This allows us to maximize the obtainable quantum efficiency by maximizing the probability of photoemission.

The importance of stoichiometry control for a high quantum efficiency is related to impact of stoichiometry control on the work function and the electronic band structure. As it influences the formation of surface dipole layers that change the potential barrier, it can enhance the probability of photoemission and thus increase the overall quantum efficiency [27]. Especially influential is the control over the ratio of the incident fluxes of Cs and Sb during film growth [23], highlighting the importance of real time rate monitoring, as well as the advantage of co-evaporation over sequential evaporation.

Although the minimum work function mentioned in Table 2.1 is associated with a 3:1 ratio for Cs_3Sb, it has been shown that the peak of photoemission, and therefore the maximum quantum efficiency, is actually at a small ratio offset [27, 28]. In Pavlenko et al., this is set at a few percent less Cs [23], meaning that it would require rate control with an accuracy of a few percent from the 3:1 flux ratio to achieve maximum quantum efficiency. However, as will be explained further in sections 3.2.2 and 3.2.3, the evaporation method and rate monitoring setup do not allow for such precision. Therefore, we aim to get within 10-20 % of the optimal ratio.

Aside from the stoichiometry, we know from section 2.2.2 that the quantum efficiency rises with the increasing thickness of the photocathode. However, this is only up to a certain thickness, indicating the peak of the photoemission. More concretely, in Stam et al,. the relation between the QE and thickness is established as $QE = a(1 - \exp(-x/b))$. Between a film thickness of about 20 and 30 nm, the QE increases by approximately 1 %, with the the curve flattening rapidly at larger thicknesses. Based on this, the films that are grown during this project are between a few and tens of nanometers, allowing us to approach the optimal thickness for maximizing the quantum efficiency, while avoiding significant photoemission decrease due to excessive growth.

Although Cs_3Sb is reported to have a QE of more than 10 % [21], this result was obtained with pulse-laser deposition. This growth method offers significantly more precise stoichiometry control during deposition than thermal co-evaporation. Therefore, we choose to adopt a more attainable QE goal of 3 %, which is based on the calculations for ONEM in Marchand et al. [9].

2.4 Energy-Dispersive X-Ray Spectrometry

In order to determine the stoichiometry of the grown thin films, we use energy-dispersive X-ray (EDX) spectrometry, where the electron beam of the LEEM acts as an excitation source. By detecting X-ray emission that is generated in the samples, we can infer the elemental composition from the produced X-ray spectra and thus make statements about the stoichiometry control during evaporation.

When the primary electron beam of the LEEM interacts with the Cs and Sb atoms that make up the thin film, the electrons undergo both elastic and inelastic scattering. One of the processes that occurs is ionization of the atoms, where the primary electrons can cause core-level excitation and consequently, relaxation of higher energy level electrons through the emission of X-ray photons. The X-ray signal can then be detected to form an X-ray intensity spectrum of the sample. Since the X-rays are characteristic

to the atomic number Z and the electronic transitions of that atom, the positions of the intensity peaks in the spectrum can be compared to known emission line energies. This then allows us to identify the elements in the sample [29, 30]. For this project, we compare the measured peaks to the Cs and Sb emission line energies that are recorded in the 2011 X-ray booklet of the Lawrence Berkeley National Laboratory, shown in table 2.2 [31]. We specifically look at the $L\alpha_{1,2}$ and $L\beta_1$ transitions, since these are most visible in the measured spectra due to higher transition probabilities. We also note that the difference between the $L\alpha_1$ and $L\alpha_2$ energies is only 9 eV and 14 eV for Cs and Sb respectively. Since the lateral resolution of the EDX cannot distinguish between them, we use the averages of these emission line energies throughout the analysis.

Table 2.2: X-ray emission line energies (in eV) of the $L\alpha_{1,2}$ and $L\beta_1$ transitions for Cs and Sb atoms [31].

Material	$L\alpha_{1,2}$ (eV)	$L\beta_1$ (eV)
Cs	4264	4611
Sb	3592	3843

The generation of X-ray emission is a probabilistic process, mainly depending on two factors: The interaction cross-section and the transition probabilities between electronic states. The interaction cross-section describes the interaction volume of the primary electron beam with the sample, as shown in Fig. 2.3. When the primary electrons reach the sample surface, they interact with the atoms through multiple elastic and inelastic scattering events, leading to a statistical distribution of events rather than well-localized interactions. This results in a tear drop-shaped interaction volume that depends on both the atomic number Z and the primary beam energy E. The size and shape of this volume describe the spatial range over which X-rays can be generated. Since the number and the type of scattering events vary throughout this volume, the detected X-rays originate from different depths and lateral positions within the region, leading to an inherent uncertainty in the exact location of X-ray generation. The penetration depth of the primary electrons can be estimated as

$$D = \frac{0.0276 \cdot A \cdot E^{1.67}}{\rho \cdot Z^{0.89}} \quad [\mu m], \tag{2.4}$$

where A is the atomic mass and ρ the density of the sample [32]. While the penetration depth can give an estimate of the maximum depth at which there is a probability of X-ray generation, it cannot describe the added complexity due to lateral scattering of electrons and the spatially varying probability of ionization inside of the interaction volume. To account for these factors, Monte Carlo simulations are often used to model the electron trajectories.

In addition to characteristic X-ray generation, another process that significantly contributes to the measured spectrum is the generation of continuum X-ray photons. This refers to emission due to inelastic interactions between primary electrons and nuclei, producing continuum X-rays — or "bremsstrahlung" — that spans over the full energy range. In the measured X-ray spectrum, this shows up as a spectral background. In addition to X-ray emission, the primary electrons can also cause the ejection of bound electrons. In this process, the energy that is released during the relaxation of higher energy level electrons is transferred to other bound electrons, which are emitted as

Auger electrons if they gain sufficient kinetic energy. The production of Auger electrons decreases the probability of X-ray generation, since it adds a competing non-radiative method for electron de-excitation [29, 30]. Due to the complications from multi-scattering events and the different types of processes that contribute to the X-ray intensities, the peak heights in the measured X-ray spectra are not directly proportional to elemental compositions of the samples. Therefore, we must account for these effects through corrections in order to perform quantitative X-ray analysis.

2.4.1 ZAF Corrections for Quantitative Analysis

Quantitative analysis of the elemental composition of samples is based on the proportionality between the X-ray intensity I_i and concentration C_i of an element i. We can quantify the amount of the element present in the material by comparing its concentration to that of a so-called "standard", which is a reference material containing a known amount of the element, measured in the exact same conditions as the unknown. The relation between the unknown and the standard is given by the *k*-ratio:

$$k_i = \frac{I_{A,i}}{I_{S,i}} = \frac{C_{A,i}}{C_{S,i}}.$$ (2.5)

Here, $I_{A,i}$ and $C_{A,i}$ represent the characteristic X-ray intensity and elemental concentration of element i in the unknown material, while $I_{S,i}$ and $C_{S,i}$ refer to those in the standard. Without corrections, eq. 2.5 is insufficient (even as an approximation) to meaningfully relate the elemental concentration to the measured peak intensity, necessitating the application of corrective procedures [30]. A popular analytical approach to these corrections is referred to as the 'ZAF method', where different corrective terms are multiplied with the *k*-ratio to increase the accuracy of the elemental concentration:
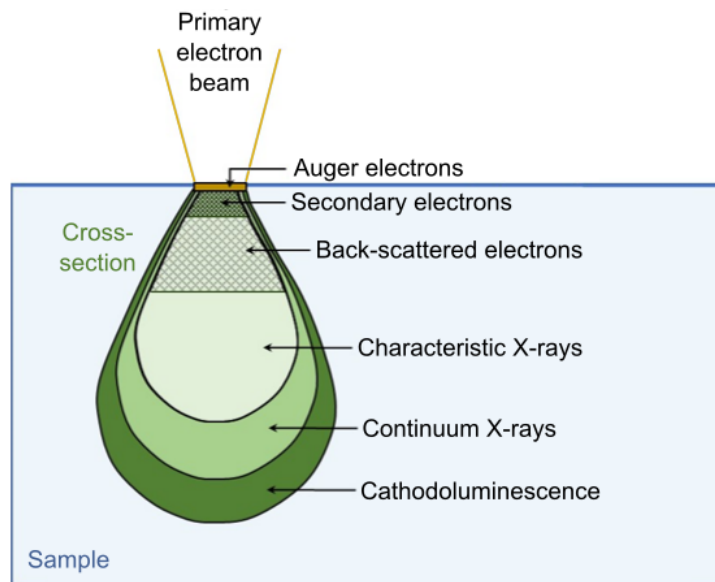

Figure 2.3: Interaction volume | Schematic of the interaction volume of a primary electron beam with a sample. The cross-section of the interaction volume describes the probability of different types of emission, such as characteristic and continuum X-ray emission [33] (modified).

$$C_i = k_Z k_A k_F k_i. \tag{2.6}$$

These terms specifically correct for different matrix effects that arise from multi-element samples, since they affect the measured X-ray intensities. The three most important corrections to consider are:

1. **Atomic number correction (Z):** This correction accounts for the differences that arise from the electron scattering and the energy loss between the sample and the standard. Specifically, it compensates for variations in electron back-scattering and the stopping power, which both depend on the average atomic number $\overline{Z}$ of the sample. The electron stopping power can be defined as the energy that is lost per unit path length inside the sample, meaning that it depends both of the sample density ρ and also on a term that describes the mean ionization potential of the material. Compensating for this is important, because an increase in the stopping power leads to less X-ray generation. The Z-correction also accounts for the dependence of the ionization cross-section on the primary beam energy and the composition of the sample.

2. **Absorption correction (A):** This term compensates for the attenuation of the characteristic X-rays that must pass through the sample in order to reach the detector. Since the primary electron penetration depth, and therefore the possible X-ray generation depth, varies with beam energy and composition of the sample, this affects the escape path length of the X-ray photons. As they travel towards the surface, there is a possibility of photoelectric absorption, which reduces the measured intensity. Even small differences between the unknown and the standard in the absorption can lead to significant changes in the measured composition. One way to reduce this is by minimizing the absorption path length through lowering the acceleration voltage of the electron beam, since this reduces the penetration depth and therefore limits the absorption.

3. **Fluorescence correction (F):** As mentioned, when samples contain multiple elements, primary or continuum X-rays generated from element i can cause excitation of bound electrons in element j, producing secondary fluorescence in the process. This causes an increase in the detected intensity of certain transition lines in element j that is not related to the actual composition. The fluorescence correction accounts for these interactions.

Together, these corrections can increase the accuracy of the k-ratios of the elements to provide better estimations of their concentrations inside the sample. In practice, implementing ZAF corrections is not trivial for multi-element, non-homogeneous materials. For example, standards must be close in composition to the unknown. Additionally, the accuracy of the concentrations is further influenced by parameters that are specific to the used experimental setup, meaning that it is important to measure the standards and unknowns in identical conditions. ZAF corrections are often combined with other procedures, such as Monte Carlo simulations, to model electron scattering trajectories and X-ray generation paths, thereby enabling more accurate determination of the ZAF terms.

2.4.2 X-ray Spectral Analysis

The ESCHER LEEM is equipped with a functioning EDX setup. Here, we consider post-measurement data processing and analysis. The emitted X-ray signals are detected as voltage pulses and recorded with a multi-channel analyzer (MCA), which bins the pulses into discrete energy channels and outputs a histogram that represents the X-ray intensities as counts over the recorded energy spectrum. The raw X-ray data is shown in blue in Fig. 2.4. As mentioned before, this spectrum contains both the characteristic and the continuum X-ray signal. In order to reduce the contribution of the latter, the Clayton algorithm is applied to estimate the bremsstrahlung and statistical noise, producing a background that can be subtracted from the spectrum. Note that in the residuals plot, there is a slight peak that most likely corresponds to the Lβ_2 transition line of Sb, which has an energy of 4.1 keV. We choose not to include this emission line in the analysis because it does not show up in most of the spectra that are recorded during this project. Aside from background removal, we also apply a Savitzky-Golay filter, which smooths out the X-ray spectrum using polynomial fitting in multiple windows, thereby removing some of the statistical noise contributions.

Lastly, we employ a Gaussian fitting scheme to find the most prominent peaks (see Table 2.2). This method is used due to the method of X-ray detection, which follows Poissonian statistics at large detection times (multiple minutes). This, combined with a limiting EDX resolution, leads to a Gaussian shape of the characteristic peaks, allowing us to extract the peak counts and compare X-ray intensities for stoichiometry determination.
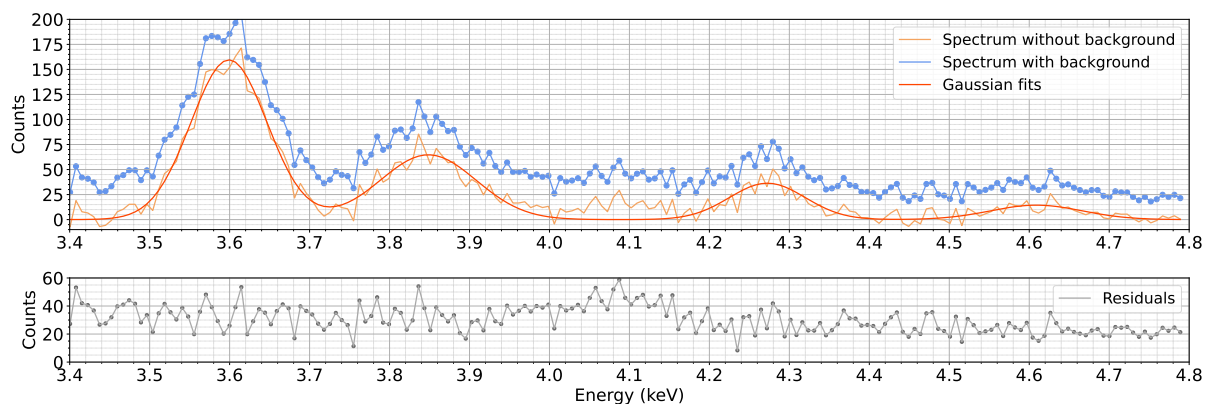

Figure 2.4: EDX data processing | X-ray emission spectrum of a Cs_xSb thin film. The blue plot shows the raw spectrum, the transparent orange plot shows the spectrum after background removal and the grey plot shows residuals. The opaque orange line corresponds to the Gaussian fits of the emission line peaks.

Experimental Framework for Photocathode Development

This chapter discusses the implementation of the setup components for characterizing both the growth process and the resulting photocathode. This then enables us to develop a film growth protocol that prioritizes photocathode functionality for ONEM. However, before we describe the setup modifications in 3.2, we use section 3.1 to go over the current setup and define requirements for the evaporation environment.

3.1 In Situ Growth

The main chamber of the ESCHER LEEM contains a resistance evaporator that creates a Cs flux and is tunable during measurements. The substrates for this growth method are usually coated with an adhesion layer, such as chromium, to promote the adherence of the Cs layer. Although this method yields a functional photocathode, the results are sub-optimal, and the setup has multiple disadvantages. While the UHV conditions of the main chamber, which has a base pressure in the order of 10^{-9} mbar, help minimize contamination during growth and thus result in cleaner photocathodes, the evaporation process leads to an increase in pressure over time. This negatively affects the measurement conditions of the LEEM by reducing the stability of the electric field between the objective lens and the sample [15]. Another downside is the limited space for additional components, complicating the implementation of new growth characterization methods.

3.1.1 Preparation Chamber

A large portion of this project is dedicated to designing and assembling a photocathode growth and characterization setup that utilizes thermal co-evaporation of Cs and Sb. The location of this setup is referred to as the preparation chamber, and is shown in Fig. 3.1. Similarly to the main chamber, it has a base pressure in the order of 10^{-9} mbar, and is connected to the rest of the LEEM through a vacuum-tight valve. Consequently, the pressure increase due to evaporation does not affect LEEM measurements. Moreover, samples can be transferred between the preparation and main

chamber without leaving the UHV environment. This so-called 'in situ' condition can preserve the quality of the photocathodes by limiting exposure to O_2 and CO_2. These and other molecules are highly reactive with alkali-metals, causing chemical composition changes that can significantly reduce the quantum efficiency in a short period of times [34]. In fact, even under UHV conditions, alkali-based photocathodes will degrade over time, albeit much slower. Therefore, since the in situ growth requirement will allow for faster sample transfer times than would be possible with external evaporation, this is another advantage that can aid in preserving photocathode quality.

The preparation chamber has a diameter of about 25 cm and a height of about 19 cm. There are several flange tubes of varying sizes that protrude from the side and the top of the chamber, creating ample space for additional components. At the center of the chamber, there is a rotary *z*-axis transfer arm that can hold three samples. By moving samples between different transfer arms inside the LEEM, the photocathodes can be grown and measured without the risk of air exposure.

3.2 Experimental Setup Design and Assembly

3.2.1 Component Layout

Over the course of this project, several components have been installed in the preparation chamber of the ESCHER LEEM, with the purpose of growing and characterizing the photocathodes. These components include a dual-source thermal evaporator, a quartz crystal monitor setup, a quantum efficiency setup and a rotary sample transfer arm with an integrated sample heater. The layout of the components in the chamber is visible is Fig. 3.1. The relative positioning of each component is discussed in separate sections that detail their design and assembly. Here, we take into account the limitations imposed by the locations of the protruding tubes and their predetermined flange sizes.
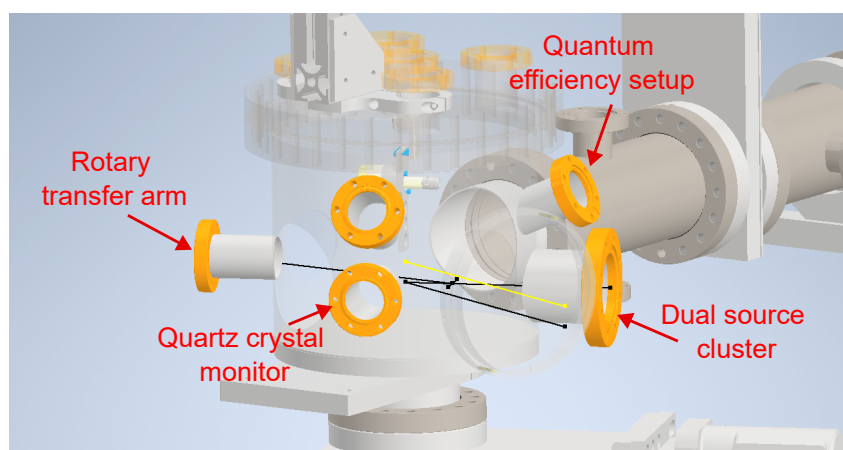

Figure 3.1: Component layout | CAD view of a portion of the preparation chamber with the positions of the installed components indicated. The co-evaporator and quantum efficiency setup are on the opposite side of the rotary transfer arm, so that they face the sample surface. The quartz crystal monitor positioned such that the quartz crystal faces the sample direction as the sample.

In addition to the components that are installed during this project, there are other pre-existing components within the ESCHER LEEM that are used to further characterize the photocathodes. Aside from measuring with the LEEM, we perform energy-dispersive X-ray spectrometry on the photocathodes after growth. We refer to section 2.4 for a breakdown of the EDX analysis.

3.2.2 Thermal Co-Evaporation

Dual Cluster Source

The cesium-antimonide photocathodes are grown using thermal co-evaporation, where each material is inside an effusion cell, or a crucible, that acts as a basket heater when a current is applied. The specific evaporator that we use is the MBE Dual Cluster Source (DCS), which contains two cell-clusters that are shielded from each other with a metal barrier. Fig. 3.2 shows a schematic drawing of the full DCS and zooms in on the two crucibles at one end of the evaporator. The cell-clusters are thermally isolated, enabling independent temperature control of each crucible without significant thermal cross-talk. The shield that sticks out on the end serves to prevent cross-contamination of the fluxes of the two materials during simultaneous evaporation. Additionally, each crucible is equipped with a rotary shutter, creating the ability to block the flux stream from entering the vacuum room during evaporation. This is useful for tuning the separate evaporation rates of the materials.
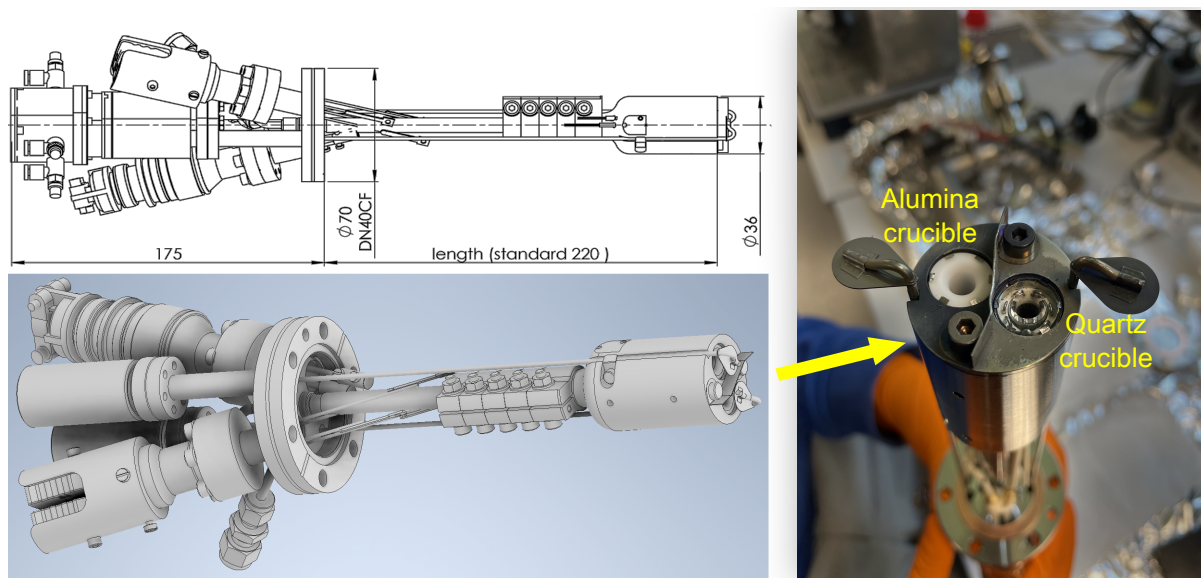

Figure 3.2: Co-evaporator │ Schematic drawing and CAD view of the MBE Dual Source Cluster evaporator with dimensions. The circle zooms in on the cell-clusters, which contains a quartz and alumina crucible. The image on the right-hand side shows a top view of the crucibles, with the shutters visible.

The crucibles inside of the cell-clusters are cylindrically shaped holders for the evaporation materials. They have a capacity of 600 mm^3, but are usually only filled less than halfway to prevent the material from accidentally falling out. The material type of the crucible depends on the evaporation material used, focusing on materials that have a low reactivity. For antimony, we use 99.9% pure pellets that are put directly into an

Al_2O_3 (alumina) crucible. Pure cesium however has the low melting point (29°C) and is highly reactive, making it difficult as well as hazardous to handle. Therefore, we use the more stable Cs_2MoO_4 (cesium molybdate), which is crushed and placed into a quartz crucible.

DCS Extension Tube

The DCS is not directly installed on one of the DN40CF flange tubes that protrude from the side of the preparation chamber. Instead, we design and fabricate an extension tube that goes in-between the preparation chamber and the DCS. There are several reasons for this, the first being the consideration of the distance between the crucibles and the substrate. The DCS supplier places the ideal source-sample distance between 100 and 160 mm. As is visible in Fig. 3.2, the distance between the DN40CF installation flange and the crucibles is 180 mm. Since the preparation chamber has a radius of about 125 mm and the protruding tube on the side of the preparation chamber is about 75 mm, this only leaves 20 mm between the source and sample.

Another reason for the extension tube is that it can be designed in such a way that the DCS can be installed at an upward angle. This is a necessary precaution to prevent the materials from falling out of the crucible when they are heated and start melting, as this would risk contaminating the interior of the UHV chamber. The DCS is also tilted upwards to ensure that the flux streams of the materials are aligned with the substrate, which is approximately 20 mm higher and located at the center of the chamber. The extension tube is designed to be approximately 81 mm and has an upward angle of 10°. This aligns the source and sample and puts their distance in the optimal range. 10° is also estimated to be sufficient to prevent the materials from falling. In Fig. 3.3, a schematic drawing of the extension tube design is shown, alongside an image of the installed extension tube and DCS.
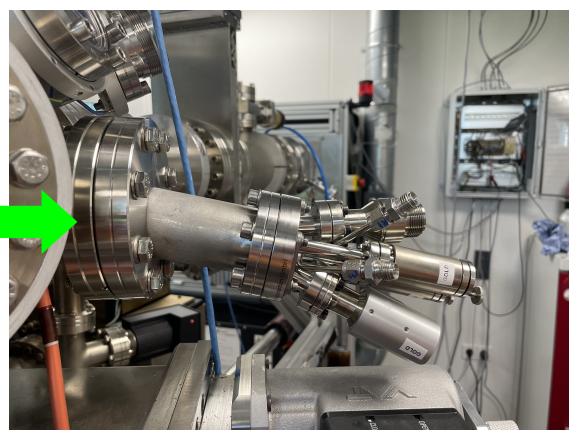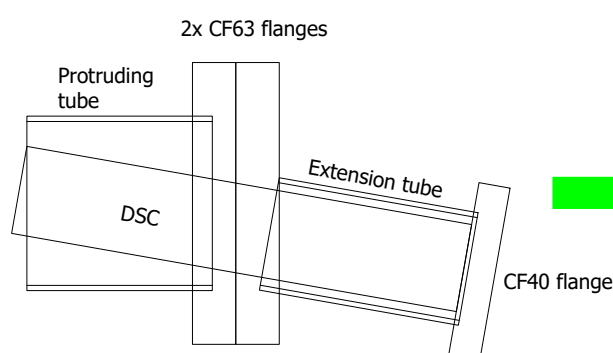
Figure 3.3: Extension tube | Schematic drawing and realization of the installation of the Dual Source Cluster on a CF63 flange using the extension tube. The size and angle of the extension tube ensure that the crucibles face the sample directly and puts them at an ideal distance from the sample.

Temperature Control of the Evaporator

Once the extension tube and the DCS are installed and leak-tested, each source is electrically connected to two separate power supplies to enable crucible heating. The Sb

and Cs sources are connected to their own separate Delta Elektronika DC power supplies, with one of the power supplies having a built in PID temperature controller (Eurotherm 3500 series). Both power supply voltages are maximized during evaporation. The currents however are carefully set, with the resulting temperature changes monitored through the temperature controller.

Most evaporation runs during this project were conducted without using an additional temperature controller. The Eurotherm 3500 series temperature controller only has one input slot, allowing for only one crucible temperature to be monitored at a time. Moreover, the controller lacks the ability to log temperature or voltage values, so during evaporation runs, temperature changes were only recorded manually at inconsistent intervals. Another issue with the temperature controller is that it cannot display measured voltage values, only temperature. The thermocouples inside the DCS are type C (W5%Re/W26%Re) , but the controller is not configured for this type, and we were unable to adjust the settings accordingly. As a result, we do not know how the controller converts the measured voltage to temperature, leaving its calculation method unclear. This makes the absolute temperature values unreliable, leaving us to only monitor the relative temperature changes to estimate the conditions inside the crucibles.

Aside from electrical connections, the DCS is also connected to a water cooling system that provides a flow of 30 L/hour. The primary purpose of this is to minimize temperature crosstalk between the sources, allowing for one crucible to reach 1300°C while the other remains at 150°C. During one evaporation run, a temperature difference of $\Delta T = 25°C$ was observed when switching the cooling system off and on. These effects demonstrate that keeping the water cooling system on during evaporation runs significantly improves control over the crucible temperature, and therefore the evaporation rate. With water cooling, the manually recorded temperatures are somewhat consistent, with small fluctuations of a few degrees.

Evaporation Tests and Calibration

During initial evaporation tests, we set the Sb source current to 3.1 A and the Cs source current to 4.2 A. As a result, the temperature displayed on the controller begins to rise from approximately 30°C. By alternating between the Sb and Cs thermocouple cables connected to the temperature controller, we can read the temperature of the Sb crucible, T_{Sb}, to be 427°C. When rotating the shutter away from the Sb crucible, T_{Sb} drops to 424°C, suggesting that the shutter likely increased the pressure inside the crucible by blocking the flux. The temperature of the Cs crucible, T_{Cs}, rises to 574°C. While we observe a dramatic change in temperature as a result of increasing the current, it is not possible to tell if the materials are being evaporated without a system that can monitor the flux rates. Therefore, the next section describes the addition of a quartz crystal monitor to the evaporation setup.

3.2.3   Quartz Crystal Monitor

To measure the Cs and Sb flux rates and the film thickness during deposition, we use a quartz crystal monitor (QCM). An image of the device is shown in Fig. 3.4. The QCM works by using the piezoelectric properties of a quartz crystal that is encased by

a crystal holder. By applying a voltage, the quartz crystal can resonate at a frequency of 6 MHz at an initial crystal health of 100%. As material is deposited on the crystal, its mass increases, causing a decrease in the resonance frequency of the crystal. The frequency shift, ΔF, is proportional to the mass change, M_f, in the following way:

$$\frac{M_f}{M_q} = \frac{(\Delta F)}{F_q}. \tag{3.1}$$

Here, M_q and F_q represent the mass and frequencies of the uncoated crystal respectively. With a frequency resolution of 0.03 Hz, the mass change can be monitored precisely, translating to a measured thickness and rate resolution of 0.037Å. The equation for calculating the film thickness is more complex than Eq. 3.1, accounting for the acoustic properties of the resonating quartz and film system. It partially depends on a parameter Z, which changes depending on the material that is deposited.
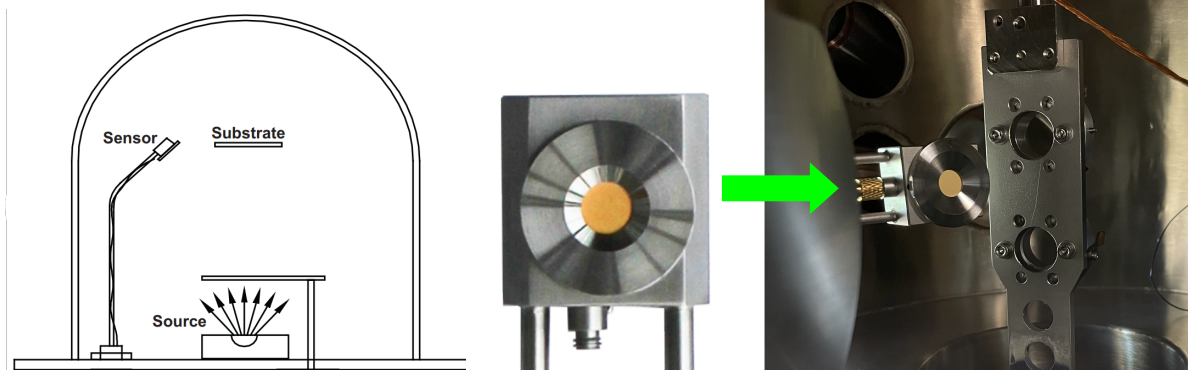

Figure 3.4: Quartz crystal monitor | The quartz crystal monitor is installed horizontally in the evaporation chamber, such that it faces the evaporation source at a slight angle and is approximately 20 mm from the center. Performing a back-of-the-envelope calculation shows that the crystal is coated evenly.

Easy Rate Single Sensor

The exact QCM that is used for this project is the Inficon Easy Rate Single Sensor. From Fig. 3.4, it is visible that the crystal holder is attached to stainless steel water tubes, providing a water cooling system for the crystal during evaporation. This makes the QCM operable in an environment of 300°C. Using bored-through union fittings, the length of the water tubes can be altered prior to installation, allowing for exact positioning of the crystal with respect to the center of the chamber (where the substrate is located). However, since the union fittings are not compatible with a UHV environment, it is advised by the suppliers to limit the number of times that the tube lengths are re-adjusted.

After installation, the center of the crystal is approximately 20 mm from the chamber center and equidistant from the evaporator sources. This distance gives the closest proximity to the sample while maintaining a safe distance to avoid contact. Of course, this means that the crystal has a slight angle θ relative to the source normal.

We can use the Knudsen cosine law, given by $P(\theta) = P_0 \cos(\theta)$, to estimate the probability of emission at an angle θ relative to the source normal. A consideration with θ

is that it cannot be too large, since this could lead to uneven deposition on the crystal surface, leading to the possibility of extra oscillation modes that bring the crystal frequency out of resonance. For a distance of 20 mm between the crystal and sample, $\theta \approx 9°$, so $P(\theta) \approx 99P_0$. From this "back-of-the-envelope" calculation, we can conclude that the difference between the deposition masses on the substrate and crystal is negligible, ensuring that the QCM is in close enough proximity. Additionally, since most of the crystal surface is covered by the crystal holder (see fig. 3.4), the diameter of the exposed crystal surface is significantly smaller than that of the entire crystal. Consequently, the angle difference between the sides of the exposed crystal is negligible compared to θ, leading to the conclusion that any oscillation modes due to uneven deposition can be ignored.

Outside of the preparation chamber, the QCM is connected to an STM-2 Thin Film Rate/Thickness Monitor. It can measure with a 0.10 s interval and logs the timestamps, crystal health percentage, rate (Å/s), film thickness (kÅ) and crystal frequency (Hz). The STM-2 software requires the user to set a density and Z-ratio of the deposited material. The density of Cs_3Sb is around 4.6 g/cm^3. The Z-ratio of Cs_3Sb is not readily available, but if the crystal health remains around 90% life or higher, the error from an incorrect Z-ratio is negligible, so this value is kept at 1.

Rate Control Limitations

After the installation of the QCM and measurement software of the STM-2, we notice that the measured evaporation rate has a relatively high noise level. For the evaporation runs where there is a sample present in the preparation chamber, we calculate the average standard deviation to be $\sigma_{av} = 0.13$ Å/s. In Fig. 3.5, the standard deviations of each run is shown. The blue dots indicate that there is no substrate positioned in the chamber (and thus do not represent any measurements in the results), and the red dots indicate that there is a substrate. σ_{av} only includes the latter, on the basis that the initial runs are used to test the performance of the QCM and evaporator setup and are not relevant for photocathode characterization.
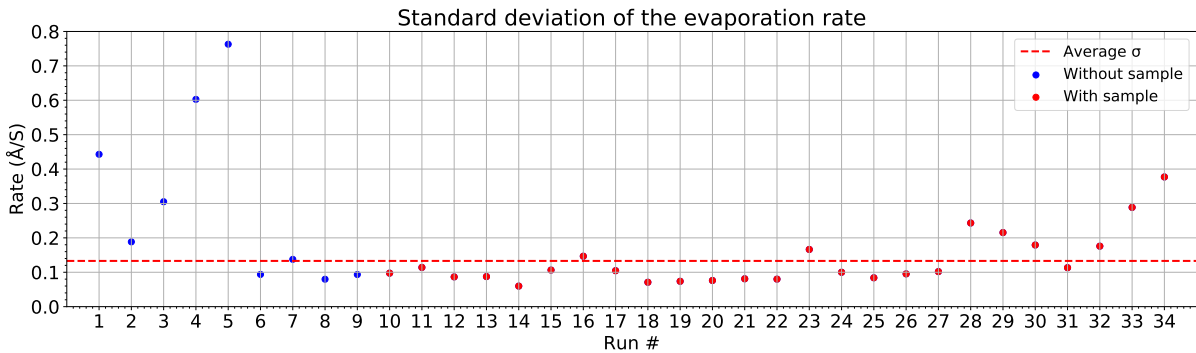
Figure 3.5: The standard deviation of the measured evaporation rate of the quartz crystal monitor, for each evaporation run that occurred during the project. The blue dots indicate measurements without sample. These therefore do not contribute to the results of this project. The red lines indicate measurements with a sample present in the evaporation chamber.

In order to figure out the source of the noise, we investigate several potential contributions. Connecting the QCM water cooling to the main water cooling system of the ES-

CHER LEEM does not produce a noticeable change in the noise levels, suggesting that excessive crystal heating is unlikely to be the cause. Large variations in mechanical vibrations from the environment outside the preparation chamber also do not result in measurable changes in noise. Furthermore, swapping the BNC cable, which connects the STM-2 to the electrical feedthrough of the sensor, shows no difference, indicating that electrical noise or signal degradation is likely not the source.

The noise levels in the evaporation rate impose a limit on the minimum evaporation rates. In Pavlenko et al. [23], the evaporation rates are in the order of $0.01\,\text{Å/s}$, which is an order of magnitude smaller than σ_{av}. Therefore, we adopt higher evaporation rates during growth. Specifically, our target rate is $0.1\,\text{Å/s}$ for Sb and $0.3\,\text{Å/s}$ for Cs, for a total deposition rate of $0.4\,\text{Å/s}$. These rates are chosen with the purpose of achieving a 3:1 stoichiometry of Cs to Sb.

Although higher evaporation rates are possible, they cause the materials in the crucibles to deplete rapidly. For instance, at $0.3\,\text{Å/s}$, the Cs crucible is depleted after approximately five runs. Each depletion necessitates us to vent the preparation chamber to ambient pressure in order to refill the crucibles. This results in significant downtime, along with an overnight bake-out process to restore UHV conditions. Additionally, material outgassing during the subsequent evaporation run increases the chamber pressure to above 1×10^{-6} mbar, further compromising the UHV environment.

Given that the target evaporation rates are on the same order of magnitude as σ_{av}, we choose to monitor changes in thickness rather than the evaporation rate. The real-time thickness graph is significantly smoother, because it is calculate from the rate using integration, thereby suppression the noise through time-averaging. By calculating the thickness change over specific time intervals, we can estimate the evaporation rate at any given moment during the growth process. In Fig. 3.6b, the rate that is calculated from the thickness (red) is shown together with the measured rate. The figure also shows the measured rate after averaging the data values to smooth out the noise (blue). Given that the red and blue lines overlap completely, we can conclude that by using the rate from the thickness, we can get an accurate estimate of the actual rate.

However, there are still several challenges that prevent us from accurately controlling the stoichiometry of the grown thin films. One issue, which is mentioned in section 3.2.2, is the fluctuation of the displayed temperature by a few degrees. A more important issue however, is that the evaporation rate decreases over time when the evaporation temperature is stable. An example of this is shown in Fig. 3.6a. At the beginning of the evaporation process, both shutters are open and the displayed crucible temperatures remain stable within a few degrees. Despite this, the red line, which shows the increase in film thickness, shows a clear decline in the deposition rate. This is also visible in 3.6b.

For a portion of the evaporation runs, we can attribute the declining rate at stable temperatures to the gradual depletion of the materials in the crucibles. This depletion complicates the reproducibility of the growth and stoichiometry between different runs, even when identical currents are used. Strangely enough, we also see this effect right after refilling the crucibles, indicating that there is another contribution to the rate decline that is not immediately clear.

Moreover, throughout the evaporation runs, it becomes clear that we are not evapo-
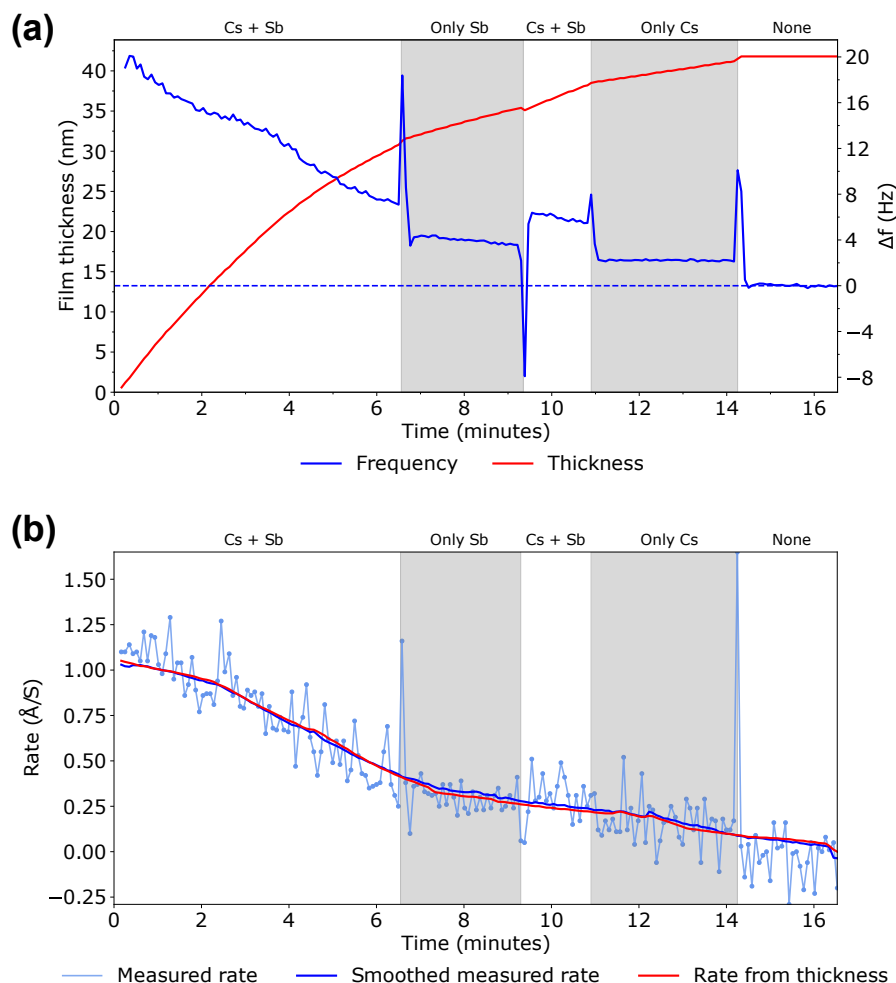
Figure 3.6: (a) Measure of the film thickness growth (in nm) on the quartz crystal during evaporation of Cs_xSb and the corresponding frequency changes (in Hz). The white and grey boxes indicate opening and closing of Cs and Sb shutters, which cause spikes in the frequency. **(b)** The evaporation rate (in Å/s) measured by the QCM during the evaporation. The transparent blue graph shows the raw measured data and the opaque blue graphs shows the data after averaging to smooth it out. We can also calculate a rate from the measured thickness, which gives a comparable smoothing of the evaporation rate.

rating the intended amount of Cs, and instead are most likely significantly below the evaporation rates that we aim for. One of the reasons for this is that we have not correctly calibrated the QCM, meaning that the actual film thickness is most likely no the same as the measured film thickness. While this has obvious consequences for the thin film characterization and quality, we can still compare the measured film thicknesses to each other.

Film Growth Protocol

After initial evaporation tests, we can establish the electrical currents and voltages of the power supplies to approximately achieve the target rates. For Sb, this is a current of 3.15 A and a voltage of 2.20 V. At these values, the displayed temperature stabilizes around 415°C. For Cs, the current and voltage are 4.20 A and 3.70 V respectively, and the displayed temperature is approximately 540°C. With these values, it is assumed

that the materials in the crucibles are not yet near depletion.

The first step in the growth process is to heat up the crucibles while the shutters are closed, so that any flux is blocked from entering the chamber. The substrate is transferred to the preparation chamber and rotated in such a way that it is angled approximately 180° from the evaporator sources. This is because, while both shutters are closed, a small evaporation rate can be detected through the QCM.

Before evaporating on the substrate, we tune the rates of the individual materials by opening one shutter at a time, and adjusting the power supply current. Then, both shutters are closed again before rotating the substrate to face the evaporator. The result of opening both shutters is visible in Figs. 3.6a,b, which show approximately 30 nm of thin film growth with a rate that ranges between 1.0 and 0.4 Å/s. Such a decrease in the rate may be attributable to the overshooting of the crucible temperature when the shutters are closed, and the subsequent decrease when the shutters initially open. However, since the depletion of the materials likely also influences the decrease in rate, it is difficult to ascertain the source of the rate reduction.

Another thing that is visible from the Figs. 3.6a,b is the abrupt change in rate due to the opening and closing of shutters. Each time the shutter position is changed, it is accompanied with a spike in the frequency change. This could be due to the sudden increase in the temperature and pressure, causing a fluctuation in the oscillation of the crystal. However, this remains speculative.

3.2.4   Quantum Efficiency Setup

A crucial part of the characterization process of the evaporated thin films is to get a measure of the photoemission performance, since this parameter is ultimately used to assess the photocathode quality and usability for ONEM. Therefore, we measure the external quantum efficiency of the photocathodes in a cathode-anode setup, a part of which is already in place before the start of the project [35].

Aside from electrical connections and units, the QE setup consists of two separate parts: One installed inside the evaporation chamber, and the other mounted on the exterior of the preparation chamber. Inside the chamber is a custom-designed anode on a rotary arm. It can be manually and precisely positioned to put it as close to the sample as possible without touching the electrically grounded sample holder. To further promote close proximity to the sample without obstructing the laser beam path, the anode is designed with a U-shape geometry. Ultimately, the separation of the sample surface and the anode is about 1-2 mm. Currently, we do not know exactly how much the cathode-anode separation affects the measurements, and therefore if a 1 mm variance is significant. This is also not easily extracted from the results, since there are multiple parameters that strongly affect the QE. It is therefore worthwhile to consider measuring the effects of the separation in future.

Electrical connections from the anode are fed through a feedthrough flange on top of the evaporation chamber, which is externally connected to a Keithley 2450 source measure unit (SMU). The SMU operates at its maximum voltage of 40 V throughout all of the measurements. Since the sample holder is grounded, this results in a 40 V potential difference between the anode and the cathode. One thing to note is that,

since we are at the maximum voltage of the SMU, it is unclear whether a higher bias voltage would increase the measured current, or whether the detection efficiency is already saturated at this voltage. During QE measurements, the current is logged by the SMU and later on converted to a quantum efficiency through:

$$QE = \frac{I_{\text{anode}} \cdot E_{\text{photon}}}{P_{\text{laser}}}. \tag{3.2}$$

Here, the QE is measured in percentage, the I_{anode} (in A) is the measured current from the SMU, E_{photon} (in eV/C) is the photon energy of the laser light and P_{laser} (in W) is the laser power. The second part is installed on a compact optical stage that is mounted on a CF40 flange viewport. It consists of a FISBA READYBeam Ind1 laser and a collimator, which are connected by an optical fiber and positioned such that laser beam aligns with the middle of the sample surface. The laser has three different wavelength options: 450 nm, 520 nm and 660 nm, with a tolerance of 5-10 nm depending on the wavelength. In order to compare these wavelengths effectively, we want to be able to measure on all three settings in one evaporation run. This is achieved by running a program that cycles through the different colors and includes a step where the laser is turned off, with each full cycle lasting around 12 seconds. Since the laser has a 3B safety classification, we choose to limit the laser power to 50 %, which is in the order of tens of mW, as this is enough to measure a difference in the photocurrent. Together with appropriate safety glasses, this precaution ensures proper laser safety without significantly compromising the results of the QE measurements.

Of course, since we direct the beam into a UHV system through a window, not all of the photons that leave the laser reach the sample surface. In order to account for the reflection and absorption of the photons on the window, we measure its transmittance and adjust the calculation of the QE accordingly. Here, we assume that the transmittance stays relatively constant throughout the project, on account of the placement of the optical stage on a flange that is outside of the range of the evaporator. After adjustment, the QE is multiplied by a factor 1.25 to account for the window.

3.2.5 Sample Transfer and Heating

Before the start of the project, the evaporation chamber contained a static sample holder that was mounted on the ceiling of the interior. This component is replaced in favor of a horizontal rotary transfer arm with sample holder and integrated sample heater. There are several reasons for this change, the first being the requirement for electrically grounding the sample holder for the QE measurements. Additionally, to introduce the possibility of investigating crystallization of Cs_3Sb thin films through epitaxial growth, we want to install a sample heater with multiple electrical connections for both heating and temperature monitoring. This necessitates a new sample holder that can accommodate for the electrical connections and the heater. By using a rotary transfer arm, we can implement these changes without compromising the ability to transfer samples from and to the rotary z-axis transfer arm.

Rotary Transfer Arm

The linear-rotary transfer arm with DN40CF feedthrough is acquired from a third party and allows for a linear adjustment of the sample position by 100 mm, which is necessary for sample transfer. Additionally, this added degree of freedom also allows us to optimally position the sample with respect to the anode and the normal axis of the evaporator. Ultimately, this position is determined to be the center of the evaporation chamber, so 125 mm from the interior walls and 127 mm from the crucibles. By installing the transfer arm on a flange that is opposite to the evaporator, we can ensure that the grown thin films are deposited uniformly on the sample surface. Aside from the transfer arm itself, we also install a port aligner on the CF40 flange, which can be used to make millimeter adjustments to the position of the transfer arm in the plane perpendicular to the linear movement, thereby facilitating in alignment during sample transfers.

When extended, the transfer arm has a length of 130 mm, which would be enough to reach the chamber center. However, we realize that this is not actually the case, since we also need to consider the 75 mm distance between the flange and the inner walls due to the protruding tube, and additionally the port aligner, which adds another 70 mm. Consequently, we require an extension piece on the transfer arm that is at least 140 mm long. There are several design requirements to be considered for the extension piece, such as UHV compatibility, a weight load limit on the transfer arm and the insulating properties of the material. The latter is a requirement for installing a heater at the end of the extension piece, since we want to prevent thermal coupling between the heater and the transfer arm itself. In order to satisfy these requirements, we opt for a 100 mm MACOR (ceramic glass) extension piece with a 40 mm heating element attached to it. The MACOR piece is a solid cylinder with a diameter of 10 mm, and can be heated to more than 100 °C on one side for extended periods of time without heat transfer to the other side. The extension piece after installation on the transfer arm is shown in Fig. 3.7.

Sample Holder and Heating

In Section 2.3.1, we determine a goal substrate heater temperature of $80 - 90$ °C, based on previous research work. Based on this goal, we decide to design and build the heating element in-house. It consists of a cylindrical copper piece with a step that creates two different diameters. We choose copper because of its high thermal conductivity. One side (11.4 mm) is attached to the MACOR extension piece, while the other side (10 mm) is threaded in order for a sample cap to be screwed on. Through this, we ensure that the sample cap is properly thermally coupled to the sample cap, and thus indirectly to the sample. The copper piece is heated by four $75\,\Omega$ resistances. By interfacing the conducting surfaces of the resistances with the copper piece and securing them tightly with screws, we attempt to create as much surface contact as possible. However, since this method does not guarantee perfect contact, we assume that only 50 % of the surfaces actually thermally coupled when we calculate the required heating power. Additionally, we use one of the screws to electrically connect the a ground wire to copper piece, and thereby ground the sample for QE measurements. The resistances are connected in series to a Delta Elektronika power supply through a feedthrough flange. Aside from this, we also connect a type K thermocou-
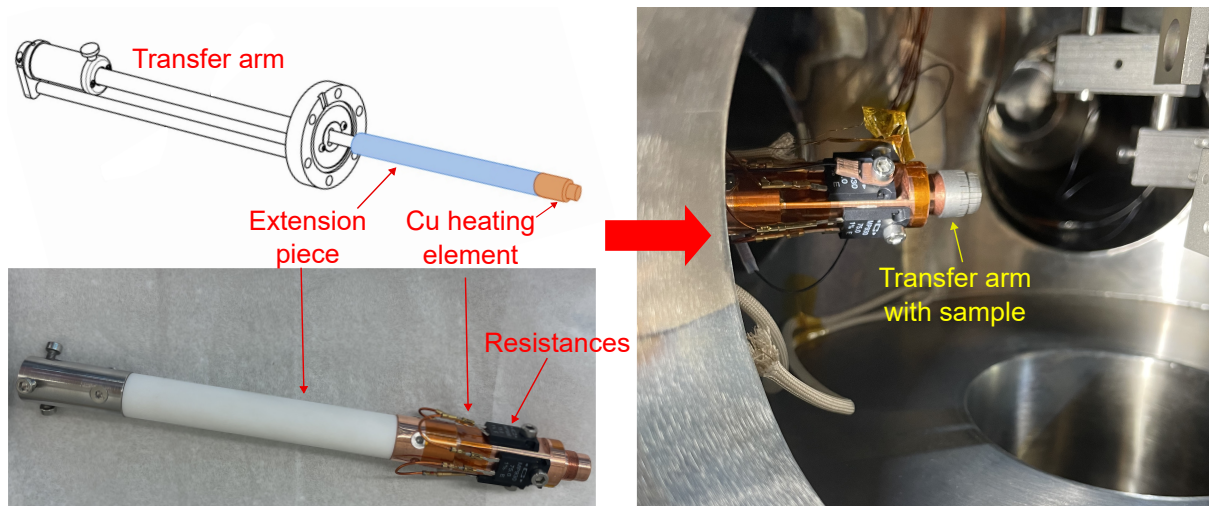
Figure 3.7: Transfer arm | Schematic drawing and realization of the rotary transfer arm with MACOR extension piece and copper heating element. The copper element is in contact with in series-connected resistances and a type K thermocouple. A sample cap can be screwed onto the end of the copper element, indirectly connecting the heater to the sample surface.

ple (Nickel-Chromium / Nickel-Alumel) to the heating element. By connecting the thermocouple to an OMNI temperature controller through the feedthrough flange, we can monitor the temperature of the heating element. To ensure that the wires inside the evaporation chamber do not electrically couple, we wrap the exposed connections in insulating Kapton tape, as is visible in Fig. 3.7.

Another important thing to note is that, while we can reach a maximum temperature of around 82 %, this does not necessarily mean that the sample is also at this temperature. This is because the sample cannot be directly thermally coupled to the heating element, meaning that thermalization takes much longer. It is difficult to make an estimation on this, since we cannot guarantee proper surface contact between the resistances and the copper, and the cap and the sample.

Although we do not have an exact temperature to aim for, it is still important that the sample heater can be stabilized to allow for future investigation of optimal sample heating temperatures. While this was not achieved during this project, we therefore recommend implementing a PID control system to the sample heating process. More importantly however, the OMNI controller cannot be calibrated for a type K thermocouple, meaning that we can only monitor temperature changes, rather than exact temperatures. Lastly, we did not implement temperature logging during this project, meaning that it is currently only digitally displayed. Overall, while the groundwork for the sample heater has been laid, there are clear improvements to be made in future.

Film Growth Characterization and Optimization

Section 3.2 describes the measurements components that are used to characterize the photocathodes and evaluate their suitability for the purpose of ONEM. This chapter presents and discusses the results for multiple photocathodes, measured both during and after evaporation. Here, we mainly focus on the photoemission and the stoichiometry control through QE and EDX, and attempt to link this to film thickness and growth rate adjustments that were measured by the QCM. Furthermore, we compare the photocathodes to each other and discuss variations in the quality that arise from changes in the growth conditions — such as the achievable growth rate and chamber conditions — as well as the limitations in characterization in the current measurement setup.

4.1   Quantum Efficiency Measurements

The quantum efficiency serves as a primary measure of the photocathode quality, making it an important marker in the characterization and optimization process. While comparing QE values across photocathodes is straightforward, the variations in the QE can arise from multiple factors, such as the film thickness and the stoichiometry. Therefore, aside from comparing overall magnitudes, we link the QE to the QCM measurements to get more insight into how the QE curves evolve with changes in the evaporation rate. This way, we can better characterize the grown photocathodes and identify optimization steps.

4.1.1   Blue Light QE During Evaporation

Figs. 4.1 show the QE results from three different evaporation runs, labeled run A, B and C, which were done consecutively within one week of each other. The left-hand side figures show how the QE (in percentage) and film thickness (in nm) evolve over time in run A, B and C respectively. In these runs, only the blue laser (450 nm) is turned on, operating at 50 % laser power, or approximately 20 mW. This is because during these runs, it was not yet possible to cycle between different laser colors. Since
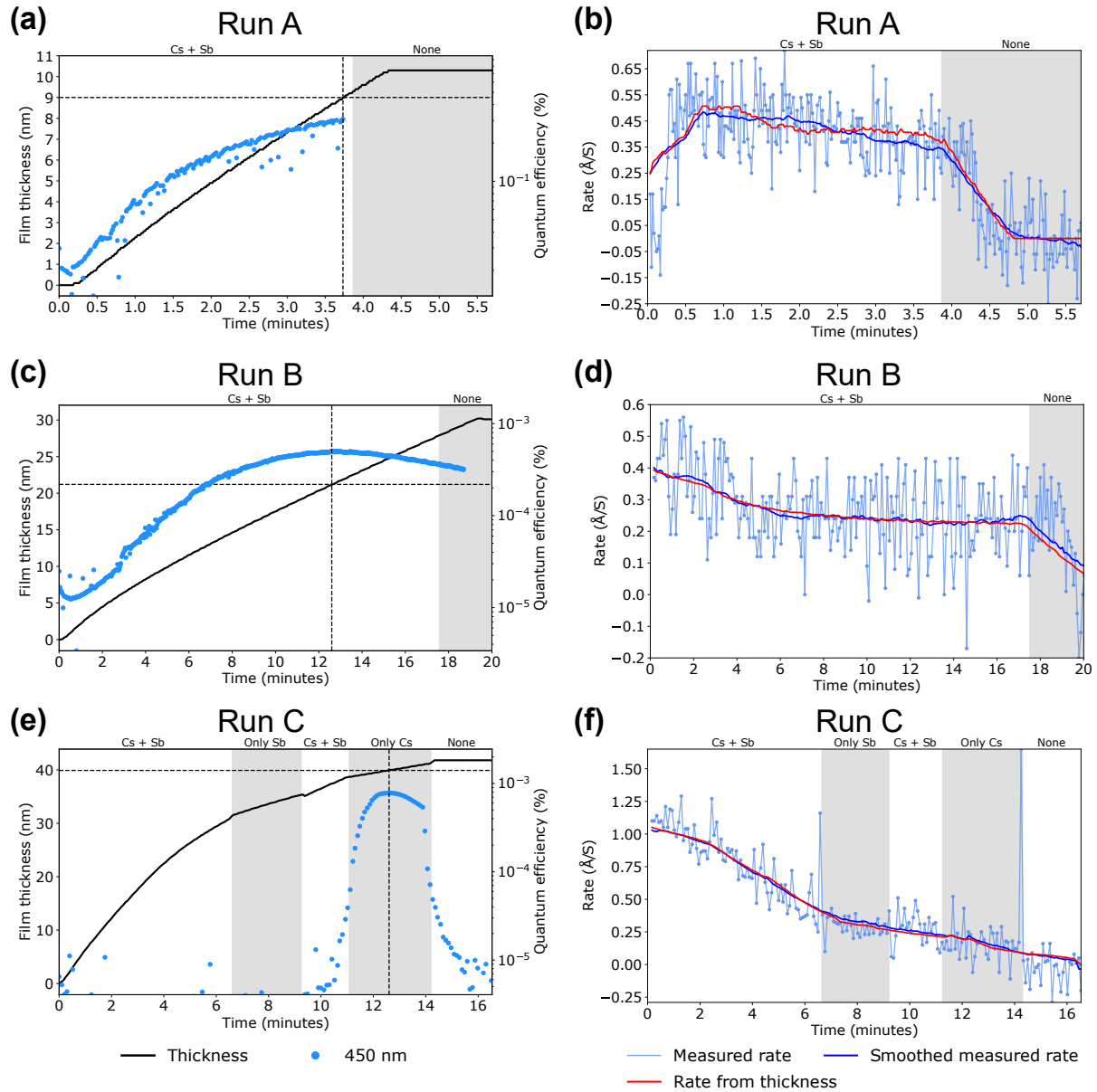
Figure 4.1: QE and QCM | Graphs of the measured quantum efficiency over time during evaporation, for multiple runs. The figures on the left-hand side show QE (in percentage) and the film thickness (in nm) vs time (in minutes), and the figures on the right-hand side show the evaporation rate (in Å/s) in the same time frame. The measured evaporation rate is plotted as raw data and after averaging, together with the calculated evaporation rate from the measured thickness. **Figs. a, b** correspond to run A, **Figs. c, d** to run B and **Figs. e, f** to run C.

the blue laser has the highest photon energy, we use this in the initial measurements to get the highest possible QE values. In section 4.1.2, the red and green light laser are also turned on, enabling QE comparison at different wavelengths.

The right-hand figures show how the overall evaporation rate change (in Å/s) over time. We note that there are three different evaporation rate plots: The measured rate shows the raw data that is extracted from the quartz crystal monitor, while the smoothed measured rate shows the same data after averaging. Since the averaging was done post-evaporation, we used changes in the film thickness to manually mon-

itor the rate changes during the evaporation runs. Therefore, the thickness has been converted to a rate and plotted as well. As is visible in the right-hand figures, the averaged rate and the rate extracted from the thickness do not show much difference.

QE Magnitude Comparison

The first thing that we can see from the QE measurements is the difference in the order of magnitude between run A and run B/C, which is approximately 10^{-3} % at the highest point of each QE curve. This is a significant change, revealing that while all runs are done in the same setup, the growth conditions can majorly impact the photoemission quality between thin films. The maximum QE of run A, which is 0.3 %, comes closest to the 3 % QE goal that is formulated based on Marchand at al. [9]. It is however still an order of magnitude lower. Most likely, this is because of a lack of Cs compared to Sb, meaning that the stoichiometry does not have a 3:1 ratio.

One of the main issues that hinders proper stoichiometry control is the lack of rate control. Although section 3.2.3 describes a film growth protocol that aims for Cs evaporation rate of 0.3 Å/s and Sb evaporation rate of 0.1 Å/s, this is likely not the actual evaporated rate. Instead, the Cs atoms that reach the quartz crystal are quickly desorbed into the vacuum or migrate deeper into the material. As a result, the thin film layer that is grown on the substrate contains significantly less Cs than the QCM rate indicates, thereby contributing to poor photoemission and photocathode quality.

This issue persists in run B and C. It is however does not fully explain the difference in the QE magnitude compared to run A. It is important to note that, between run A and B, the evaporation chamber was vented for maintenance and to refill the Cs and Sb crucibles, meaning that we cannot attribute the lower QE in run B to a depletion of Cs. Instead, due to installation of a new component, the anode in the QE setup was positioned more than a centimeter away from the sample, directly before run B. The 10^{-3} % QE difference between run A and B can therefore be attributed to a decrease in the electrons being measured by the anode. While this issue was resolved between run B and C, several evaporation runs took place in the meantime. Consequently, the similar QE magnitudes observed in runs B and C are likely due to Cs depletion by the time run C was performed.

Effects of Growth Rate Variation on QE

Aside from the magnitude of the QE, we can examine the change in the QE as it evolves in time. It is especially interesting to connect how the QE increases and decreases due to changes in the evaporation rate, and the opening and closing of Cs and Sb shutters.

The transitions from white to grey blocks in Figs. 4.1 indicate the opening and closing of the shutters, with the shutter configuration for each block specified above the figures. Fig. 4.1b shows that run A starts with a relatively steep rate increase, which is reflected in a QE increase as the film grows to 3 nm. The rate increase at the start of the run is due to the overshooting of the crucible temperature while both shutters are still closed. Once they are opened, the higher temperature causes a higher starting rate, after which it decreases by about 0.15 Å/s until the shutters are closed again. The rate decrease is visible in the QE curve, which becomes less steep and almost plateaus around 9 nm.

While we expect to see the QE plateau as the thin film reaches an optimal thickness at the maximum photoemission, this is most likely not the case in run A. Instead, we think that the decreasing QE is the result of a decreasing Cs evaporation rate over time. In fact, we suspect that this is what happens in run B and C as well. Figs. 4.1b, d, f all show a significant rate decrease over time. From the shutter position changes in run C, we can see that this is not because the Sb evaporation rate decreases, as the rate plateaus somewhat when only the Sb shutter is open.

Aside from the decreasing Cs rate, it is clear from each run that we are not evaporating Cs and Sb in a 3:1 ratio. Instead, the grown layer lacks enough Cs to be a Cs_3Sb photocathode. This is also a contributing factor to the QE magnitude being lower than expected. The lack of Cs in the thin film layer is most visible in run C, where Fig. 4.1e shows that the QE only starts decreasing rapidly once the Sb shutter is closed and the Cs shutter is left open. This sudden steep increase indicates that almost 40 nm of growth is mostly Sb, after which the layer is caesiated for another few nanometers. As soon as the Cs is also closed, the the QE decreases to zero within a couple of minutes. We would not expect such a rapid decrease from a Cs_3Sb photocathode. In actuality, the Cs atoms partially diffuse into the Sb thin film and are partially desorbed into the vacuum. Therefore, we can argue that this run does not actually demonstrate co-evaporation, but rather sequential evaporation of Sb and Cs, leading to a significant limitation in the maximum achievable photoemission.

Consequently, the thicknesses that are associated to the peaks in the QE curves in the runs are not attributable to an optimal film thickness at maximum photoemission. This agrees with the fact that none of these thicknesses match, instead differing in tens of nanometers. As a result, we cannot comment on the relation between the thickness and the QE, as we do not find a value at which the film thickness becomes too large.

4.1.2   QE on a Biological Sample

In subsequent evaporation runs, it became possible to cycle between different laser colors. Runs D and E in Figs. 4.2 show the results of cycling between blue (450 nm), green (520 nm) and red (660 nm) laser light The laser also cycles between being on and off. Their QE curves are plotted in the the corresponding colors. The figures in Figs. 4.2 have the same layout as Figs. 4.1.

Unlike runs A-C, which use standard Si/SiO_2 substrates, runs D and E use an ITO-coated fused SiO_2 substrate, which is overlaid with a 40 nm layer of mouse brain tissue. Specifically, run D is done on the backside of this substrate and run E on the frontside (with the biological tissue). The thin films grown on each side are comparable in thickness, i.e. about 8 nm.

Starting with run D, represented by Fig. 4.2a, we can see that the QE for each laser color increases from zero as soon as both shutters are opened. After 5 nm of growth, the Sb shutter is closed and the backside of the sample is caesiated until a thickness of about 8 nm is reached. During the caesiation, the QE does not increase nearly as rapidly as when both shutters are open. We find that the blue curve reaches about 5×10^{-3} %, which is two orders of magnitude lower than the maximum QE at a comparable thickness in run A. Unlike with run C, this cannot be attributed to Cs depletion, since the crucibles were refilled shortly before run D. Instead, we find from Fig.
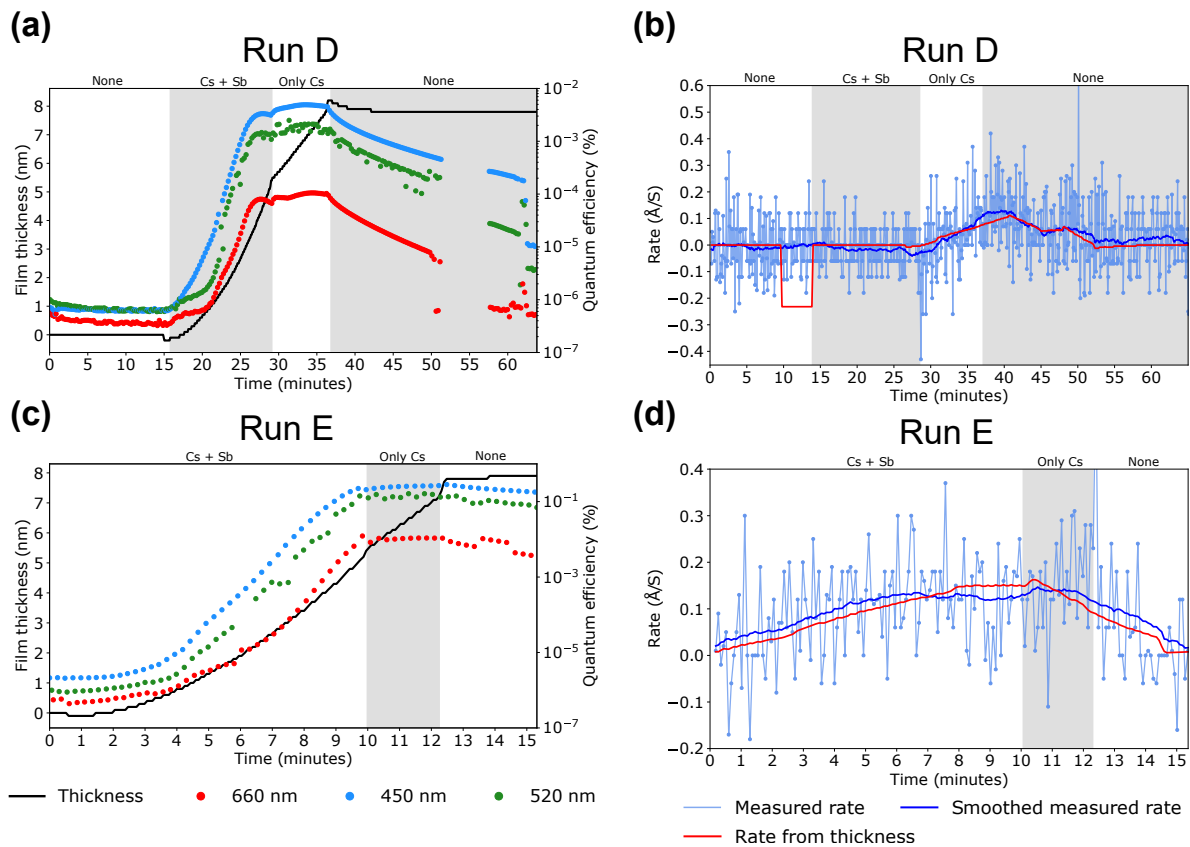
Figure 4.2: QE and QCM | Graphs of the measured quantum efficiency over time during evaporation, for multiple runs. The figures on the left-hand side show QE (in percentage) and the film thickness (in nm) vs time (in minutes), and the figures on the right-hand side show the evaporation rate (in Å/s) in the same time frame. The measured evaporation rate is plotted as raw data and after averaging, together with the calculated evaporation rate from the measured thickness. **Figs. a, b** correspond to run D and **Figs. c, d** to run E.

4.2b that the evaporation rate is below 0.1 Å/s during co-evaporation; this is significantly lower than the rate in run A. Although the rate is low, the QE is still an order of magnitude higher than in run B, even though the rate in run B was higher and the crucibles were also refilled. This can be attributed to a better stoichiometry in run D. This conclusion is made based on the fact that closing the Sb shutter significantly changes the slope of the QE curve, indicating that we are not necessarily cesiating on a mostly Sb thin film. Another clue that suggests better stoichiometry is that the QE in run D decreases by about an order of magnitude in approximately 30 minutes, while the QE in run C decreases multiple orders of magnitude in a couple of minutes. This is a strong indication that the diffusive effects of the Cs atoms into the lower layer are not as significant as in previous runs, and therefore the stoichiometry of this thin film is closer to 3:1 than before. The reason why the stoichiometry appears to be better is because during run D and E, we did not use the previously established rate tuning values. Instead, we increased the power of the Cs power supply and decreased that of the Sb to test whether we could grow a layer with more Cs. This was not done in a controlled manner, and so we cannot comment on concrete currents to improve the stoichiometry.

run E, shown in Fig. 4.2c, has a blue light QE that is comparable to that of run A, with a maximum value of about 0.2 %. Similarly to run D, it shows an increase in the QE during co-evaporation, and a plateau during cesiation. We can therefore come to the same conclusion about the stoichiometry as in run D. Furthermore, the reason why the QE is more than an order of magnitude higher than in run D is because the rate was increased to almost 0.2 Å/s by turning up the Cs rate (see Fig. 4.2d). This means that the stoichiometry in run E is even better than in run D, thereby confirming that the stoichiometry significantly contributes to the maximum achievable photoemission. Indeed, we see in Fig. 4.2c that after both shutters are closed, the QE goes down by less than a factor of 2 in the following minutes. While this measurement does not last as long as that of run D, we can see in Fig. 4.2b that the blue light QE goes down more rapidly in approximately the same amount of time. Consequently another that the stoichiometry is better a decrease in the rate degradation of the photocathode through Cs diffusion into the thin film. Overall, compared to run A-C, we can assume that we are indeed co-evaporating in run D and E, leading to an improved blue light QE.

Laser Color Comparison

Cycling between laser colors allows us to look at more realistic conditions of ONEM, since the intent is to use wavelengths of 520 nm and especially 660 nm in order to cause no significant damage over time.

We can see from Fig. 4.2a that the green laser light QE reaches the same order of magnitude as the blue one, with it's peak being a factor 3 smaller than the blue peak. Given that the difference between the level of damage at the two different wavelengths can be significant, this is a relatively small difference between the QE values. In Fig. 4.2c, we can see that this difference is even smaller, with the maximum QE of the green laser being comparable to that of the blue laser. Naturally, this is a very promising result for ONEM. There is larger difference when we compare these curves to that of the red light laser. Fig. 4.2a shows that the maximum QE of the red laser is nearly an order of magnitude smaller than that of the green laser. In run E, this difference again appears to be smaller, as is about 5 times lower than the green laser peak. Still, this means that the red light peak is nearly in the order of 10^{-2} %, which is two orders of magnitude away from the QE goal of 3 %. Given that ONEM is at a very early stage, this makes the red light QE result promising within current expectations.

4.1.3 Blue Light QE Post-Evaporation

In between run B and run C, we performed a run where we evaporated a sample with a 30 nm thin film layer. Before this run, the anode was moved back to the previous position, about 1 mm away from the substrate. While we measured the QE during evaporation, we used this run to test measuring with green laser light, and found that the measured QE current would not increase beyond 0.4 nA. This converts to a QE that is in the range of 10^{-6} %, and is significantly lower than subsequent measurements with green laser light. Instead of increasing, the value remained approximately constant during the entire evaporation process.

We switched to the blue light laser shortly before evaporating, consequently bringing the QE up by two orders of magnitude. Fig. 4.3 shows the gradual decrease of

the QE over a period of approximately 1.5 hours. The intention was to continue this measurement for longer, but this became impossible due to software issues. Still, this measurement shows the degradation of the photoemission quality of the thin film for a significantly longer amount of time than the measurements discussed thus far. We can see that in 30 minutes, the QE decreases by a factor 0.1. Compared to the order of magnitude decline in run D in the same time period, this a relatively small decline. The rate of degradation remains constant, ultimately reducing the QE with about 30 % after 1.5 hours. We suspect that the degradation rate is this low because the thin film layer barely contains Cs. Therefore, the desorption rate into vacuum is low. Since we only attempted co-evaporation, and did not cesiate the sample, there is also no significant diffusion of Cs atoms into a lower layer. Therefore, the quality of photoemission, although not sufficient for the layer to be a working photocathode, does not change much post-evaporation.
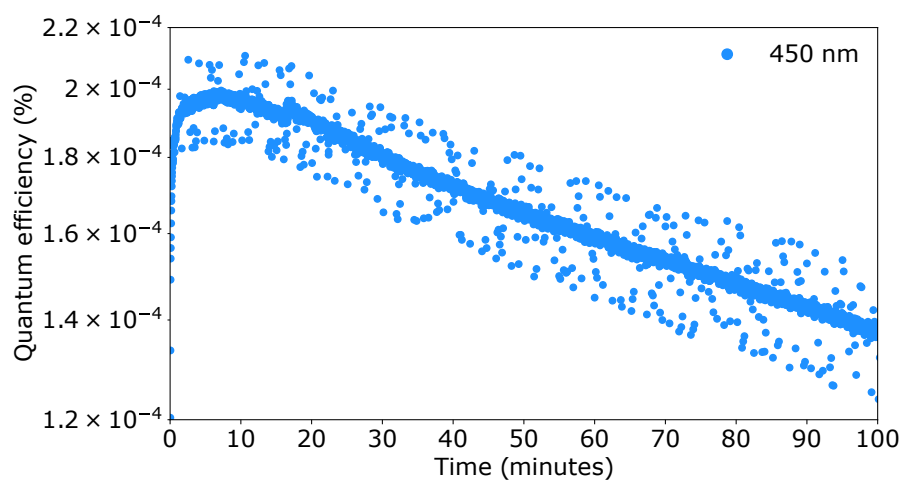

Figure 4.3: QE post-evaporation| Graph of the quantum efficiency over time post-evaporation, showing the gradual degradation of the QE of the blue light laser over the course of approximately 1.5 hours.

4.2   Film Thickness Comparison

Aside from QE measurements, we can take the X-ray spectra of the grown thin films post-evaporation to characterize the photocathode quality. The main parameter that we can examine with EDX is the stoichiometry of Cs and Sb, by looking at the count values of peaks corresponding to the characteristic X-ray emission lines of Cs and Sb, specifically at the $L\alpha_{1,2}$ and $L\beta_1$ transitions. This is because this is where the peaks were most visible, and therefore able to be fitted with a Gaussian function during analysis.

In Figs. 4.4, we compare the count value at the X-ray emission peaks for different film thicknesses, since the count is correlated to the film thickness. Fig. 4.4a shows the full X-ray spectrum with four peaks, while Figs. 4.4b-e zoom in further to examine the peaks better. The Sb peaks show that the peak count increases with increasing thickness. The peak count difference between 10.3 and 23.2 nm is noticeably larger than those between 23.2 and 30.4 nm and 30.4 and 41.8 nm. At smaller film thicknesses (~ 10 nm and below), it becomes difficult to detect enough counts to distinguish peaks

from the background noise. Consequently, only the Sb L$\alpha_{1,2}$ fitted, as the other Sb peak is not distinguishable.

Film Thickness vs Peak Counts

The peak counts of the Cs peaks do not show the clear relation between the peak height and the thickness. Instead, the 41.8 nm peaks are lower than the 23.2 and 30.4
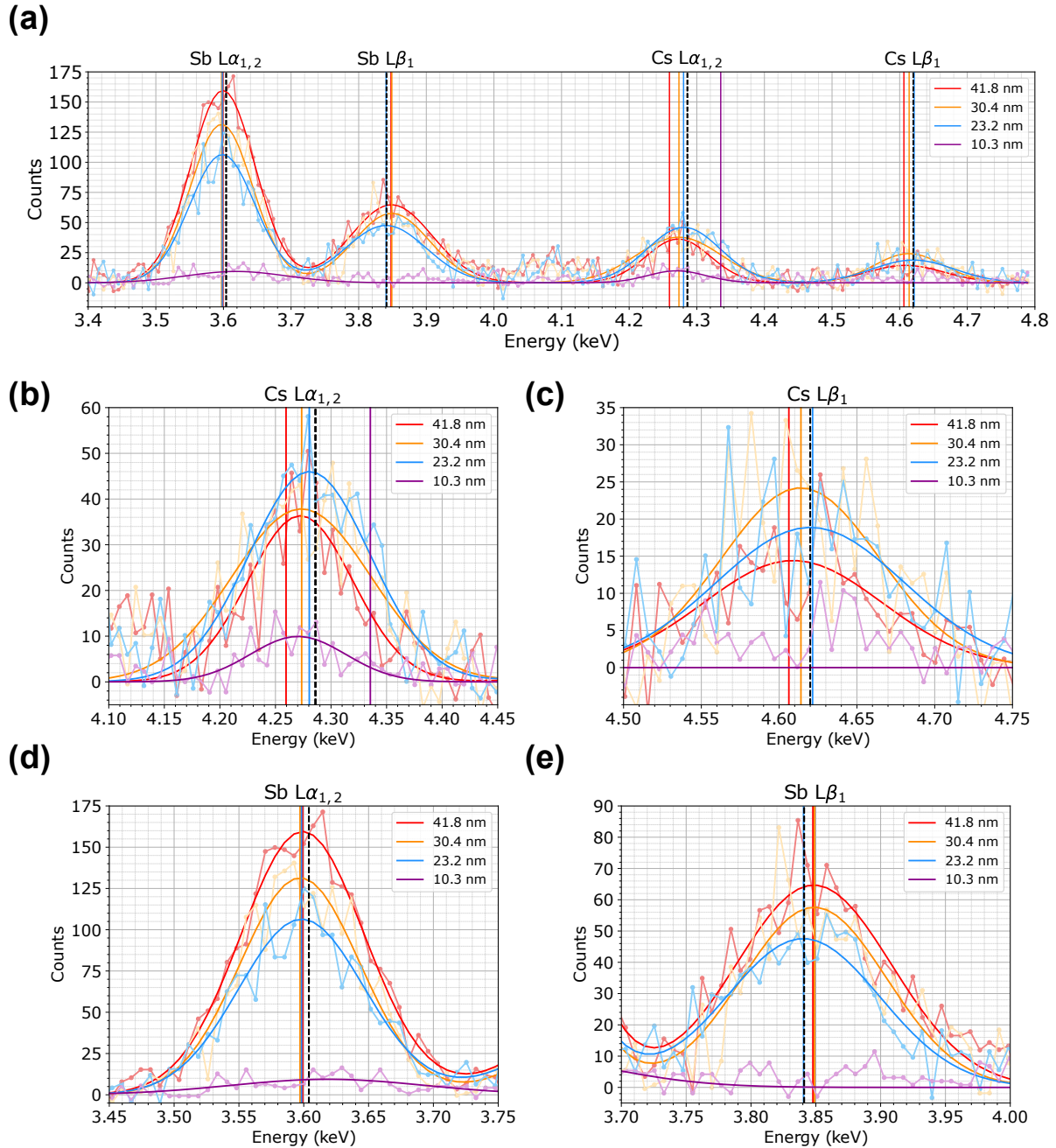

Figure 4.4: Film thickness comparison with EDX | X-ray emission spectra of evaporated thin films for different thicknesses. The transparent plots show the raw EDX data after background removal, while the opaque plots show the corresponding Gaussian fits. **Fig. a** shows the full spectrum, while **Figa. b-e** zoom in on the most prominent peaks, corresponding to the L$\alpha_{1,2}$ and Lβ_1 transitions of Cs and Sb.

nm ones. Additionally, the 23.2 nm peak has a higher peak count than the 30.4 nm peak at the L$\alpha_{1,2}$ transitions. The 41.8 nm thin film corresponds to run C, with a QE in the order of 10^{-4} % due to the depletion of Cs during evaporation. Naturally, we want to attribute the lower counts to the lack of Cs. However, this is likely not the correct conclusion. The 30.4 nm thin film corresponds to the run that is represented in Fig. 4.3, where the QE is measured post-evaporation. While the QE here is also in the order of 10^{-4} %, we concluded from the degradation rate that the thin film mostly lacks Cs atoms. Therefore, we do not expect the 30.4 nm peak count to be higher than the 41.8 nm one. Similarly, we measured a QE in the order of 10^{-8} % for the 23.2 nm thin film. This very poor photoemission quality means that this thin film likely also lacks enough Cs atoms to form a photocathode.

Instead, we attribute the lack of correlation between the film thickness and the peak count to the overall count values, which are at 1-2 orders of magnitude below expected values. Fig. 4.4a does not just show the Gaussian fits, but also the raw EDX data (transparent lines). Between the 23.2, 30.4 41.8 nm film thicknesses, the count differences in the raw data are too small to make a meaningful distinction between peak count values. The peak counts that are extracted from the Gaussian fits are not accurate enough (within 10 counts) to make meaningful conclusions about the correlation between the film thickness and the count values for the Cs peaks.

Quantitative and Qualitative Stoichiometry

While the main goal of the EDX measurements is to determine the stoichiometry of the evaporated thin films, this tasks turns out to be significantly less trivial than initially expected. Firstly, we did not perform EDX measurements on reference materials, or "standards", which are similar in composition to the evaporated thin film. Without measuring their X-ray spectra in the same setup with identical parameters, it is impossible to obtain a quantitative stoichiometry, as there are several matrix effects that we cannot correct for without comparison. This includes differences in X-ray absorption, the atomic number (and consequently, the back-scattering factor) and secondary fluorescence effects. Since the corrections for these effects depend on the composition of the reference materials, quantitative analysis is outside of the scope of this project.

In fact, it turns at that we also cannot meaningfully comment on the qualitative stoichiometry, which would be obtained by comparing the peak counts of Cs and Sb after adjusting for their mass fractions. One of the reasons for this is that the thickness of the films is too small. From eq. 2.4, we can estimate the primary electron beam penetration depth to be 1.2 μm at 10 keV, which means that the electrons reach far into the substrate, and consequently, most of the detected X-rays originate from the substrate instead of the thin film. Since the primary electrons lose energy as they enter the sample, there is a depth-dependence on the excitation probability.

Additionally, it is very likely that there are multi-scattering events inside of the thin film and substrate. The primary electrons undergo both elastic and inelastic scattering processes. Since inelastic events can generate secondary electrons with sufficient energy to induce further ionization, the total ionization rate becomes difficult to calculate, as the ionization volume is dependent on events that are probabilistic in nature. Therefore, it is necessary to run Monte Carlo simulations in addition to performing calibration measurements with reference materials.

Overall, the actual interpretation of the peaks remains ambiguous: When a Cs peak is detected, it is unclear how much of the detected X-rays originate from the thin film, and how much originates from Cs atoms that have diffused into the substrate. The X-ray intensity is not necessarily linearly proportional to the elemental concentration, because of the multiple effects that contribute to a non-uniformity in the local excitation probability. Instead, the measured X-ray peaks are influenced by more than just the composition of the thin film, and as a result, qualitative comparison of the Cs and Sb peak heights cannot give us a meaningful conclusion about the stoichiometry.

While far beyond the scope of this project, the outlook will address steps towards both qualitative and quantitative stoichiometry determination through EDX measurements and X-ray spectral analysis.

4.3 Effects of Sample Heating

One of the ways to improve the quality of the photocathodes is through substrate heating, which can promote epitaxial growth of Cs and Sb into a crystalline structure. In this section we look at sample heating both during evaporation and post-evaporation, while measuring X-ray spectra.

4.3.1 Substrate Heating During Evaporation

In section 3.2.5, we described the design and installation of a substrate heater on the sample transfer arm. Fig. 4.5 show the results from initial heater tests, during which we evaporated 30 nm of Cs_xSb onto a heated Si/SiO_2 sample and measured the evaporated rate with the QCM. Although temperature logging was not available during this test, we manually measured a maximum heater temperature of about 80 °C. After evaporation, we measured the X-ray spectrum of the thin film. In Fig. 4.5, we compare this spectrum (red) to the X-ray spectrum of a 30 nm thin film that was evaporated without sample heating (blue). The sample without sample heating is the same sample as was measured in Fig. 4.3, meaning that the QE for blue light is in the order of 10^{-4} %.

While we have already concluded that we cannot make meaningful comments about the stoichiometry, we can compare the peak heights per emission line. The blue Cs and Sb have a visibly higher peak count than the red peaks, differing in tens of counts. Since the layers have a similar thickness according to the QCM, this is an unexpected result, but can be explained by the effects of the substrate heating on the film thickness. The actual thickness of the heated sample is most likely smaller than the thickness that was measured by the QCM. This is because during evaporation, the higher temperature at the grown layer caused the promotion of Cs absorption into the vacuum. Since the quartz crystal was not heated to the same temperature, this effect is not visible in the readout.

Furthermore, the blue light QE of the heated sample during evaporation never reached more than 0.4 nA, converting to a QE in the order of 10^{-6} %. This suggests that the stoichiometry of the thin film is not anywhere near 3:1 for Cs and Sb. Consequently, no crystalline structures are formed that could affect the peak heights in the X-ray spectrum.
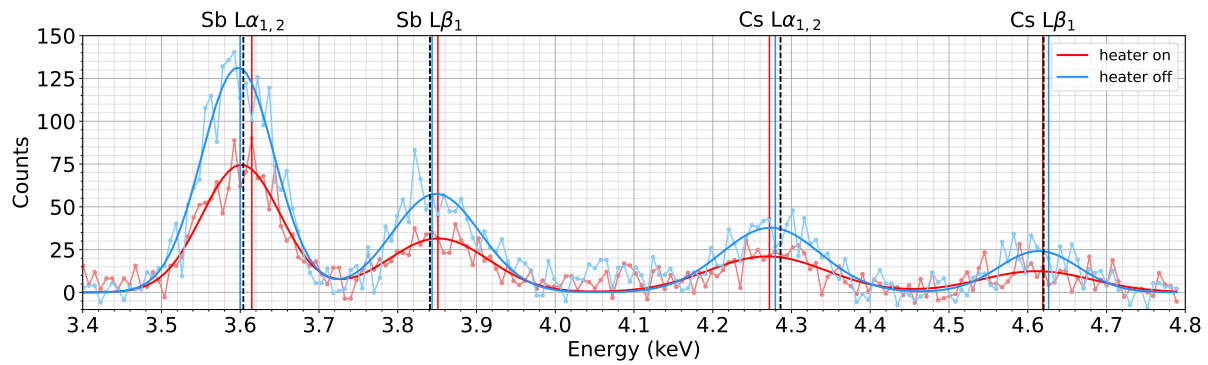
Figure 4.5: Sample heating during evaporation | X-ray emission spectra of 30 nm thin films, showing the X-ray peaks of the L$\alpha_{1,2}$ and Lβ_1 transitions for Cs and Sb. The red plot shows the spectrum of the sample that was heated to 80 °C during evaporation. The blue plot shows the spectrum of the sample that did not undergo sample heating. The transparent lines show the raw EDX data, while the opaque lines show the corresponding Gaussian fits.
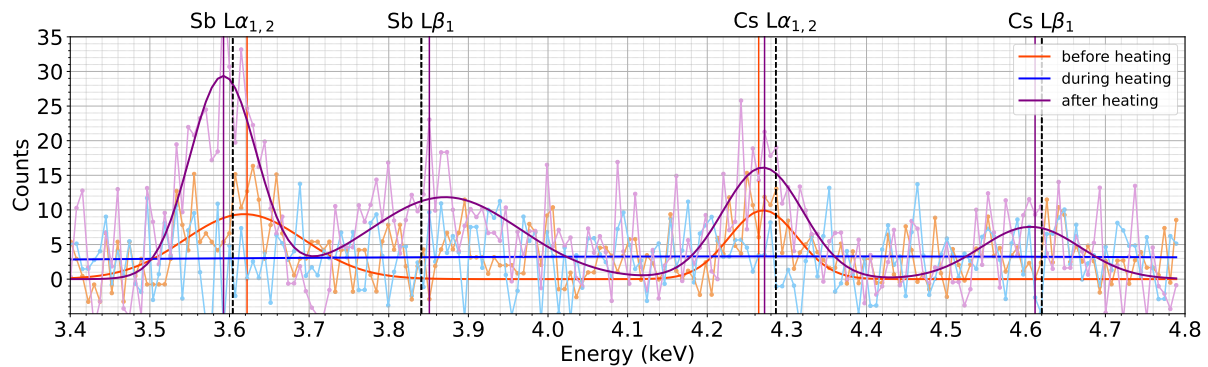

Figure 4.6: EDX before, during and after sample heating | X-ray emission spectra of the 10 nm thin film from run A, showing the X-ray peaks of the L$\alpha_{1,2}$ and Lβ_1 transitions for Cs and Sb. The three plots correspond to the spectra before (purple), during (blue) and after (orange) substrate heating using the main chamber heater. The transparent lines show the raw EDX data, while the opaque lines show the corresponding Gaussian fits.

4.3.2 Sample Heating Post-Evaporation

One of the samples was also heated outside the preparation chamber, using the heater in the main LEEM chamber. This post-evaporation heating was not intended to promote epitaxial growth. Instead, we aimed to investigate whether substrate heating after deposition would rearrange the Cs and Sb atoms in the thin film into a crystalline structure.

Fig. 4.6 shows the X-ray spectra the 10 nm of an evaporated thin film before, during and after sample heating. This film corresponds to run A, so the maximum QE of this sample is around 0.3 %. This means that it most likely has a relatively high Cs content, making its stoichiometry better than that of other samples and thus, giving it a higher chance at crystallization. While the exact temperature of the main chamber heater is unknown, the current is increased to a maximum of 2 A, which is *at least* higher than the maximum achievable temperature of the heater in the evaporation chamber.

We can see from Fig. 4.6 that the heating has a clear affect on the Cs and Sb peak

counts. Due to the relatively low count values, it is not possible to distinguish the Sb $L\beta_1$ peak and Cs $L\beta_1$ peak before heating, so they do not have Gaussian fits. This is because the sample from run A is only 10 nm thick, and as we saw before, this results in low peak counts compared to larger thicknesses. During heating, the peaks become completely indistinguishable. More interestingly, the peak counts are actually noticeably enhanced after post-heating. Specifically, the Sb $L\alpha_{1,2}$ peak increases by a factor 3 and the Cs $L\alpha_{1,2}$ increases by a factor 1.5. Moreover, both $L\beta_1$ transitions are now visible. Another thing to note is that it seems as if the Sb $L\alpha_{1,2}$ peak has shifted to a lower energy. This is however not an effect of sample heating, and can instead be explained by the error in the Gaussian fits due to the noise in the raw EDX data.

It is not immediately clear from the X-ray spectra why the peak counts are enhanced as a result sample heating. We also performed PEEM measurements on this sample; these are shown in Figs. 4.7. We see that as the sample is heated further, the surface evolves over time. In 4.7b, bright patches start to form in various spots on the film. They grow and change in shape over time, eventually turning into the shapes that are visible in 4.7c. It first, we suspected that this was a form of crystallization. However, after performing LEED measurements, we found that there are not diffraction patterns visible. Since these are characteristic to crystalline structures, we quickly came to the conclusion that thin film did not undergo a crystallization process. Instead, we suspect that the bright patches appear due to inhomogeneous Cs desorption as a result of sample heating. While the contrast changes different areas, the total image intensity does not. Therefore, the enhanced Sb peak counts could be a result of a higher Sb ratio in the film. This is however quite speculative, since we established that the peak counts do not actually fully represent the composition of the sample. Another thing to note is that the bright patches disappear in the LEEM measurements after the sample has cooled down. This indicated that the inhomogeneity of the Cs desorption only lasts while the sample is being heated.
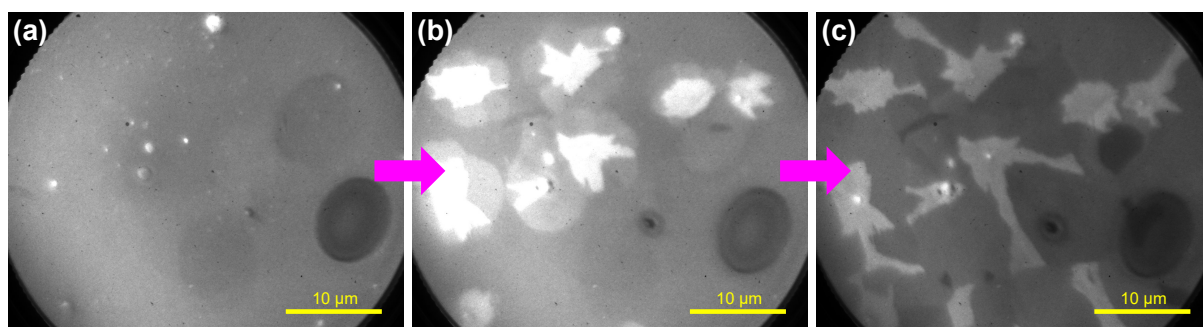

Figure 4.7: During sample heating | 45 μm field of view PEEM images that show the progression of bright patch formation on a 10 nm Cs$_x$Sb thin film during sample heating. The patch shapes and positions stop evolving as the sample is heated further. After sample heating, the patches disappear again.

4.4 ONEM Measurements

While this project is mainly focused on assembly of a co-evaporation setup and the characterization of the evaporated thin films, we performed two "proof-of-concept"

ONEM measurements to gauge the quality of the photocathodes with regard to the intended use case.

Over the course of the project, two different ONEM measurements were performed using photocathodes grown in the preparation chamber. The first sample that we measured with ONEM is a 30 nm thick $250 \times 250\,\mu$m SiN membrane that is suspended from a 200 μm thick silicon frame. On one side of the sample, a 3.2 nm Cs_xSb thin film is grown. The membrane is then imaged with ONEM, using a 405 nm laser. The wavelength of the laser is low to give a higher chance of sufficient photoemission of the photocathode. This is because, since this measurement was performed relatively early on in the project, there was no established growth protocol to enhance the photocathode quality. Fig. 4.8a shows the resulting ONEM image at a 45 μm field of view. We see a clear interference pattern. This pattern is formed by the light hitting the inner edges of the silicon frame before they arrive at the photocathode. The lateral periodicity of the pattern is around 200 nm. While the resolution appears relatively low, e.g. compared to the resolution of the LEEM, it is still promising first result.

The second ONEM measurement is performed on the biological sample from run E, therefore using the blue light laser with a wavelength of 450 nm instead of the UV-C laser. While it would be more realistic to use the green light laser, we again want to boost the photoemission of the photocathode to get a brighter ONEM image. Fig. 4.8b shows the ONEM image of the mouse brain tissue slice, again at a 45 μm field of view. The lateral resolution is sufficiently high to distinguish relevant structures in the tissue. The image shows two false-colored areas, which represent the cross sections of myelinated axons in the neurons. The ONEM image of the biological sample is an important result, as it demonstrates that while the evaporated thin films have not yet been optimized for performance, they are already usable as ONEM photocathodes.
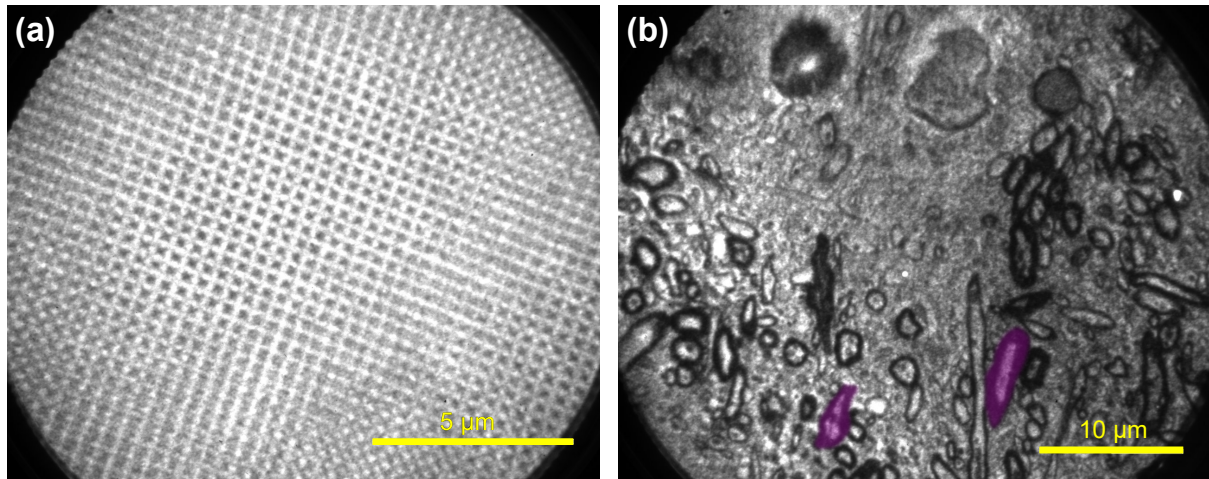

Figure 4.8: ONEM results | 45 μm field of view ONEM images of **(a)** the diffraction pattern on a 30 nm SiN membrane and **(b)** a 40 nm layer of mouse brain tissue.

Chapter 5

Outlook and Conclusion

The primary aim of this research project was to realize an in-situ co-evaporation setup in the preparation chamber of he ESCHER-LEEM, for the purpose of evaporating and characterizing Cs_3Sb photocathodes. We mainly focused on the design and assembly of this setup, with a small portion of the project dedicated to the growth and characterization of a variety of thin films — differing in film thickness and composition — in order to develop a film growth protocol that ultimately lead to the initial ONEM results.

While this goal was successfully achieved, there are still several ways to improve the setup itself, and more importantly, the conditions around the evaporation process and the methods of characterization. In this chapter, we therefore explore possible improvements and discuss further characterization steps to optimize the photoemission quality of the ONEM photocathodes.

Evaporation Rate Control

The main issue that still needs to be resolved is evaporation rate control, particularly the evaporation rate of Cs. While the Sb rate remained relatively stable throughout the project once it was fixed at a certain temperature, this was far from the case for Cs. There are several reasons for this. Firstly, the Cs salts inside the crucible deplete quicker than initially expected, usually within just a few evaporation runs. This means that most of the thin films were grown with an insufficient amount of Cs. This also necessitates venting the evaporation chamber regularly to refill the crucible. Not only does this cause delays, but it also compromises the base pressure of the chamber, which hovers around 10^{-8} mbar instead of reaching an ultra-high vacuum. Therefore, it is recommended to look into alternative Cs sources that deplete more slowly. A second issue is that, even if the crucible is not depleted, the Cs evaporation rate generally decreases over time. While we currently do not have a sufficient explanation for this, it is clear that this issue requires further investigation. Finally, we are likely evaporating much less Cs than we think. This is due to the quartz crystal monitor, which does not seem to give an accurate reading of the Cs evaporation rate. Once we started evaporating significantly more Cs than necessary according to the measured rate, we began to see noticeable improvements in the photoemission, thus suggesting that the actual Cs:Sb ratio is far below the desired 3:1 stoichiometry.

QCM Calibration

In order to obtain a more accurate reading of the Cs rate, the QCM needs to be calibrated properly. This can be achieved by performing calibration measurements to determine the tooling factor for the Cs and Sb. Since precise rate control and accurate thickness monitoring is such crucial aspects of deposition processes, we recommend incorporating the calibration into a follow-up research project. Another way to improve the rate control through the QCM is to implement real-time averaging of the noisy rate data, which would result in easier rate monitoring and tuning.

EDX for Stoichiometry

To enable both qualitative and quantitative stoichiometry determination of Cs_xSb thin films through EDX analysis, we recommend setting up a future research project to address several limitations of the current EDX setup. Firstly, it is essential to perform EDX measurements on a variety of reference materials with known compositions, including those similar enough to the Cs_3Sb thin films, in order to quantify different effects and perform proper matrix corrections. It is important that these measurements are done under identical conditions to the measurements of the thin films, in order to ensure accuracy in the comparison. Furthermore, since the penetration depth of the primary electron beam exceeds thin film thickness, it is important to investigate a way to reduce X-ray generation in the substrate. Given that ONEM requires the growth of ultra-thin photocathodes, we cannot simply increase the layer thickness. Instead, it is recommended to reduce the excitation volume by lowering the beam energy. However, this requires addressing the low count values in the measured X-ray spectra. Finally, Monte Carlo simulations can be used to model the scattering and ionization processes of the primary electron beam, which will make it easier to separate the contributions from the thin films and those of the substrates.

Further Characterization

There are, of course, more improvements that can be made, as well as other methods to further characterize the thin films. For instance, there are still multiple parameters in the setup that are not being logged, such as the the power settings that control the crucible temperatures and the temperature of the sample heater. Additionally, these systems do not have an implemented PID control system to keep the temperatures stable. Moreover, the sample heater temperature monitor is not calibrated to the correct thermocouple, which means that the temperature readout is not fully accurate. Beyond hardware/software improvements, there are important aspects of photocathode growth that remain unaddressed, such as the ultra-smooth surface requirement. By introducing techniques such as atomic force microscopy to the characterization process, we can begin to investigate the growth conditions that are necessary to produce ultra-smooth photocathodes that enhance the photoemission quality.

Future of ONEM

While there are still many aspects of ONEM that require further development, the initial results demonstrate a promising future. Given the continuation of the improvement of both the setup and the photocathodes, we expect to see significant short-term

enhancements in the lateral resolution and achievable brightness at non-damaging wavelengths. In future, the aim is to realize dynamic imaging with liquid cells, forming a next step for ONEM that has now become feasible through the steps made in this project. Overall, the results show that ONEM has the potential to be a leading super-resolution, non-invasive imaging technique.

Acknowledgments

The progress and completion of this research project would not have been possible without the help of others, so I would like to express my gratitude. Firstly, I want to thank Jay, my project partner, for his patience, since it so nicely balanced my lack thereof. I am very glad that we chose to work together, and think that we should be proud of our results. Of course, I also want to thank Guido, our daily supervisor, for his infinite helpfulness and friendliness. Together with Peter, you contributed to a very positive and motivating work environment. Other major contributors to the realization of the project were the people from the fine mechanical department and the electronics department. In particular, I would like to thank Ruud, Chris, Marcel, Peter and Raymond, who provided not just components, but importantly, lots of technical expertise that Jay and I will benefit from even after the completion of our degrees. Lastly, I want to express my gratitude towards Sense Jan. Aside from providing us with solid guidance and interesting physics knowledge, I appreciate that you are always up for challenging and insightful conversations. Overall, the environment that the Van Der Molen group and LION as a whole have fostered has instilled high standards for community and support. I can refer back to these in future, wherever that might be, so thank you for that.

Bibliography

[1] Allison M. Whited and Paul S.-H. Park. Atomic force microscopy: A multifaceted tool to study membrane proteins and their interactions with ligands. *Biochimica et Biophysica Acta (BBA) - Biomembranes*, 1838(1, Part A):56–68, 2014. Structural and biophysical characterisation of membrane protein-ligand binding.

[2] Yi Xiao and Weilin Xu. Single-molecule fluorescence imaging for probing nanocatalytic process. *Chem*, 9(1):16–28, 2023.

[3] Andrew J. Bower, Janet E. Sorrells, Joanne Li, Marina Marjanovic, Ronit Barkalifa, and Stephen A. Boppart. Tracking metabolic dynamics of apoptosis with high-speed two-photon fluorescence lifetime imaging microscopy. *Biomed. Opt. Express*, 10(12):6408–6421, Dec 2019.

[4] Soohyen Jang, Kaarjel K. Narayanasamy, Johanna V. Rahm, Alon Saguy, Julian Kompa, Marina S. Dietz, Kai Johnsson, Yoav Shechtman, and Mike Heilemann. Neural network-assisted single-molecule localization microscopy with a weak-affinity protein tag. *Biophysical Reports*, 3(3):100123, 2023.

[5] Noah Gray. Knowing the limit. *Nature Cell Biology*, 11(1):S8–S8, October 2009.

[6] Ke Xu, Hazen Babcock, and Xiaowei Zhuang. Dual-objective storm reveals three-dimensional filament organization in the actin cytoskeleton. *Nature methods*, 9:185–8, 02 2012.

[7] Kirti Prakash, Benedict Diederich, Rainer Heintzmann, and Lothar Schermelleh. Super-resolution microscopy: A brief history and new avenues. *Philosophical Transactions of The Royal Society A Mathematical Physical and Engineering Sciences*, 380:1, 02 2022.

[8] Andreas Engel. Biological applications of the scanning transmission electron microscope. *Journal of Structural Biology*, 214(2):107843, 2022.

[9] Raphaël Marchand, Radek Šachl, Martin Kalbáč, Martin Hof, Rudolf Tromp, Mariana Amaro, Sense J. van der Molen, and Thomas Juffmann. Optical near-field electron microscopy. *Phys. Rev. Appl.*, 16:014008, Jul 2021.

[10] Kevin Jensen. *Advances in Imaging and Electron Physics: Electron Emission Physics*. Elsevier, 2007.

[11] S. M. Schramm, J. Kautz, A. Berghaus, O. Schaff, R. M. Tromp, and S. J. van der Molen. Low-energy electron microscopy and spectroscopy with escher: Status and prospects. *IBM Journal of Research and Development*, 55(4):1:1–1:7, 2011.

[12] Johannes Jobst, Laurens M. Boers, Chunhai Yin, Jan Aarts, Rudolf M. Tromp, and Sense Jan van der Molen. Quantifying work function differences using low-energy electron microscopy: The case of mixed-terminated strontium titanate. *Ultramicroscopy*, 200:43–49, 2019.

[13] Maaike Westerdijk. The growth and characterisation of a thin film caesium antimonide photocathode, 2023.

[14] Alimohammed Kachwala, Pallavi Saha, Priyadarshini Bhattacharyya, Eric Montgomery, Oksana Chubenko, and Siddharth Karkare. Demonstration of thermal limit mean transverse energy from cesium antimonide photocathodes. *Applied Physics Letters*, 123(4):044106, 07 2023.

[15] R.M. Tromp, J.B. Hannon, A.W. Ellis, W. Wan, A. Berghaus, and O. Schaff. A new aberration-corrected, energy-filtered leem/peem instrument. i. principles and design. *Ultramicroscopy*, 110(7):852–861, 2010.

[16] Michael Edidin. Near-field scanning optical microscopy, a siren call to biology. *Traffic*, 2(11):797–803, 2001.

[17] Zhen Zhang, Phillip Ahn, Biqin Dong, Oluwaseyi Balogun, and Cheng Sun. Quantitative imaging of rapidly decaying evanescent fields using plasmonic near-field scanning optical microscopy. *Scientific Reports*, 3(1):2803, Sep 2013.

[18] Robert C. Dunn. Near-field scanning optical microscopy. *Chemical Reviews*, 99(10):2891–2928, 1999. PMID: 11749505.

[19] N.W. Ashcroft and N.D. Mermin. *Solid State Physics*. HRW international editions. Holt, Rinehart and Winston, 1976.

[20] Matthijs Rog. From bipeem to uv-onem: Theory and experiment. Master's thesis, Leiden University, 2022.

[21] W. G. Stam, M. Gaowei, E. M. Echeverria, Kenneth Evans-Lutterodt, Jean Jordan-Sweet, T. Juffmann, S. Karkare, J. Maxson, S. J. van der Molen, C. Pennington, P. Saha, J. Smedley, and R. M. Tromp. Growth of ultra-flat ultra-thin alkali antimonide photocathode films. *APL Materials*, 12(6):061114, 06 2024.

[22] Eugene A. Mechtly. 4 - properties of materials. In Wendy M. Middleton and Mac E. Van Valkenburg, editors, *Reference Data for Engineers (Ninth Edition)*, pages 4–1–4–33. Newnes, Woburn, ninth edition edition, 2002.

[23] Vitaly Pavlenko, John Smedley, Alexander Scheinker, Ryan L. Fleming, Anna Alexander, Mark A. Hoffbauer, and Nathan A. Moody. Stoichiometry control and automated growth of alkali antimonide photocathode films by molecular beam deposition. *Applied Physics Letters*, 120(9):091901, 03 2022.

[24] Jun Feng, Siddharth Karkare, James Nasiatka, Susanne Schubert, John Smedley, and Howard Padmore. Near atomically smooth alkali antimonide photocathode thin films. *Journal of Applied Physics*, 121(4):044904, 01 2017.

[25] Alice Galdi, Jan Balajka, William J. I. DeBenedetti, Luca Cultrera, Ivan V. Bazarov, Melissa A. Hines, and Jared M. Maxson. Reduction of surface roughness emittance of Cs3Sb photocathodes grown via codeposition on single crystal substrates. *Applied Physics Letters*, 118(24):244101, 06 2021.

[26] Susanne Schubert, Jared Wong, Jun Feng, Siddharth Karkare, Howard Padmore, Miguel Ruiz-Oses, John Smedley, Erik Muller, Zihao Ding, Mengjia Gaowei, Klaus Attenkofer, Xue Liang, Junqi Xie, and Julius KÃŒhn. Bi-alkali antimonide photocathode growth: An X-ray diffraction study. *Journal of Applied Physics*, 120(3):035303, 07 2016.

[27] Clayton W. Bates, Dhruba Das Gupta, Luis Galan, and D.N.E. Buchanan. X-ray photoemission studies of cesium antimonide photoemitters. *Thin Solid Films*, 69(2):175–182, 1980.

[28] K. H. Jack and M. M. Wachtel. The characterization and crystal structure of caesium antimonide, a photo-electric surface material. *Proceedings of the Royal Society of London. Series A, Mathematical and Physical Sciences*, 239(1216):46–60, 1957.

[29] Check out MyScope online microscopy training tool. — myscope.training. `https://myscope.training/EDS_exploreTab`.

[30] Rene Van Grieken and Andrzej Markowicz. *Handbook of X-ray Spectrometry*. CRC press, 2001.

[31] A Thomson, DT Attwood, M Gullikson Eric, et al. X-ray data booklet, centre for x-ray optics and advances light source, lawrence berkeley national laboratory. Technical report, LBNL/PUB-490 Rev. 3, http://henke. lbl. gov, 2011 Search PubMed, 2019.

[32] KA Kanaya and S Okayama. Penetration and energy-loss theory of electrons in solid targets. *Journal of Physics D: Applied Physics*, 5(1):43, 1972.

[33] Virtual Labs — emb-iitk.vlabs.ac.in. `https://emb-iitk.vlabs.ac.in/exp/sem-basics/theory.html`.

[34] Gaoxue Wang, Ravindra Pandey, Nathan A. Moody, and Enrique R. Batista. Degradation of alkali-based photocathodes from exposure to residual gases: A first-principles study. *The Journal of Physical Chemistry C*, 121(15):8399–8408, 2017.

[35] Balint Bosman. A design for real-time quantum efficiency measurements in the leem prep chamber, 2023.